ELSEVIER

Contents lists available at ScienceDirect

Science Bulletin

journal homepage: www.elsevier.com/locate/scib



Article

DHX36-mediated G-quadruplexes unwinding is essential for oocyte and early embryo development in mice

Yu-Xuan Jiao ^a, Guo-Wei Bu ^b, Yun-Wen Wu ^a, Yu-Ke Wu ^a, Bao-Bao Chen ^b, Meng-Ting She ^c, Yi-Hang Zhang ^c, Yu-Jing Lu ^c, Heng-Yu Fan ^{a,b,d,*}

- ^a MOE Key Laboratory for Biosystems Homeostasis, Life Sciences Institute, Zhejiang University, Hangzhou 310058, China
- ^b Center for Biomedical Research, Shaoxing Institute, Zhejiang University, Shaoxing 312000, China
- ^c School of Biomedical and Pharmaceutical Sciences, Guangdong University of Technology, Guangzhou 510006, China
- d Assisted Reproduction Unit, Department of Obstetrics and Gynecology, Sir Run Run Shaw Hospital, School of Medicine, Zhejiang University, Hangzhou 310016, China

ARTICLE INFO

Article history: Received 11 August 2024 Received in revised form 18 January 2025 Accepted 25 January 2025 Available online 17 February 2025

Keywords:
DHX36
G-quadruplex
Meiosis resumption
Early embryo development
rRNA homeostasis
Chromatin configuration

ABSTRACT

DHX36 plays a crucial role in regulating transcriptional and post-transcriptional processes through its interaction with G-quadruplexes (G4s). The mechanisms by which DHX36 regulates G4s vary across different cell types and physiological conditions. Oocyte-specific conditional knockout (CKO) mice were utilized to study the impact of DHX36 deficiency on female fertility. The results show that the CKO mice exhibit severely impaired hormone response, ovulation, and complete infertility. The CKO germinal vesicle (GV) oocytes display large nucleoli, aberrant chromatin configuration, decreased chromatin accessibility, disturbed transcriptome, and inhibited meiosis progression. Following fertilization, the embryos derived from the CKO oocytes arrest at the zygote or 2-cell stage. Notably, we observed inadequate rRNA transcription in growing GV oocytes, as well as insufficient pre-rRNA processing and translation activity in fully-grown GV oocytes. Using a G4 probe and antibody, we found increased G4s formation at the chromatin and cytoplasm of CKO GV oocytes; these G4s mainly originate from the rDNA and pre-rRNA. Furthermore, the distribution of DHX36 was found to be spatiotemporally synchronized with that of pre-rRNA and G4s in early mouse embryos. In vitro experiments confirmed that DHX36 directly binds with pre-rRNA through the RHAU-specific motif (RSM). Overexpression of DHX36 could partially alleviate the pre-rRNA accumulation in fully-grown CKO oocytes. In conclusion, this study highlights the physiological significance of DHX36 in maintaining female fertility, underscoring its critical role in rRNA homeostasis and chromatin configuration through G4-unwinding mechanism in mouse oocytes.

© 2025 The Authors. Published by Elsevier B.V. on behalf of Science China Press. This is an open access article under the CC BY license (http://creativecommons.org/licenses/by/4.0/).

1. Introduction

G-quadruplexes (G4s) are four-stranded secondary structures formed by guanine-rich DNA or RNA sequences in unimolecular or intermolecular configurations, which require at least three guanine tracts per strand, stabilized by Hoogsteen hydrogen bonds with monovalent cations at the center [1,2]. *In vivo* detection of G4 structures has been achieved using the G4-specific antibody BG4 [3,4]. With over 370,000 predicted G4 motifs in the human genome [5], G4 structures have been identified in various regions including the telomeric repeats [6] and gene promoters [7]. Small molecules targeting G4 structures have been developed for *in vivo* imaging and they often localize within the nucleolus [8–11].

E-mail address: hyfan@zju.edu.cn (H.-Y. Fan).

DHX36, also known as RHAU, is a member of DExD/H-box family that exhibits unique G4 binding and ATP-dependent resolvase activity [12–14] and plays a crucial role in transcriptional and post-transcriptional regulation of developmental processes, such as spermatogenesis [15,16] and heart development [17]. However, its physiological function in female fertility remains unknown.

Oocytes and early embryos exhibit dynamic chromatin configurations and transcription patterns. Oocytes with an intact nuclear membrane are known as "germinal vesicle (GV) oocytes." In growing GV oocytes (GO), transcription of mRNA and rRNA is active. During oocyte growth, transcription gradually decreases as chromatin condenses, and typical nucleoli are replaced by atypical nucleoli called nucleolus-like bodies (NLBs) [18]. Non-surrounded nucleolus (NSN) and surrounded nucleolus (SN) are two major chromatin organization states in fully-grown GV oocytes (FGO) [19]. In FGO, rDNA-containing regions coalesce to form several highly condensed foci located at the periphery of the NLBs [20].

^{*} Corresponding author.

The NLBs disassemble during meiosis resumption, and the nucleoli reappear as nucleolus precursor bodies (NPBs) after fertilization, which persist through the first four cell divisions, gradually decreasing in size from 8-cell stage, and eventually disappearing by the late 16-cell stage as typical nucleoli emerge with intermingled fibrillar and granular compartments [18,20,21].

In this study, our primary objective is to investigate the physiological role of DHX36 in oocyte and early embryo development. Utilizing an oocyte-specific conditional knockout (CKO) mouse model, in conjunction with comprehensive RNA-seq and ATAC-seq analyses, as well as employing fluorescence imaging techniques with G4 probe and BG4 antibody, we aimed to unravel the intricate relationship between DHX36 and G4 structures and their impact on RNA homeostasis and nucleolar function. Our findings unveiled that G4 structures exhibit preferential formation at rDNA regions and pre-rRNA sequences in mouse GV oocytes. The accumulation of G4 structures within chromatin-accessible regions in CKO oocytes impeded mRNA and pre-rRNA transcription, while their presence in pre-rRNA sequences disrupted proper rRNA processing, ribosomal assembly, and subsequent translation efficiency.

2. Materials and methods

2.1. Cell culture

HeLa, MOSE and HEK293T cells were cultured in Dulbecco's modified DMEM medium (Gibco, D9800-13) supplemented with 10% fetal bovine serum (TBD) and 1% penicillin-streptomycin (BI, 03-031-1B) at 37 °C in a 5% $\rm CO_2$ incubator. Upon reaching 80% confluence, cells were rinsed twice with PBS and dissociated with trypsin (Gibco, 25200072) at 37 °C for 5 min for subculturing.

2.2. Plasmid construction and cell transfection

The Dhx36 and $Dhx36^{\triangle RSM}$ were cloned into the pRK5-derived expression vector and fused with an N-terminal FLAG tag to generate the pRK5-Flag-Dhx36 and pRK5-Flag-Dhx36 $^{\triangle RSM}$ plasmids. HEK293T cells were transfected with plasmids upon reaching 70% confluence using Lipo2000 transfection reagent (Invitrogen, 11668019) according to the manufacturer's instructions.

2.3. Mice breeding and genotyping

All animal experiments were conducted according to the guidelines of the Animal Research Committee of Zhejiang University, and the experimental protocol (ZJU20210309) was approved by the Institutional Animal Care and Research Committee of Zhejiang University. The *Dhx36*^{fl/+} mouse strain (C57BL/6) was purchased from GemPharmatech (Nanjing, China). Mating and breeding were performed to generate *Dhx36*^{fl/fl}; *Zp3-Cre* female mice. Genotyping was carried out using primers listed in Table S1 (online).

2.4. Oocytes and embryo collection and culture

GO were obtained by dissecting ovaries from 2-week-old female mice and puncturing the follicles to release the oocytes. FGO were retrieved from 3 to 4-week-old female mice injected with 5 IU of pregnant mare serum gonadotropin (PMSG) for 44–48 h. The diameter of oocytes in both WT and CKO groups were measured using ImageJ software, with measurements defined according to a fixed scale bar. Each oocyte and NLB is approximated as a sphere, with volume calculated using the formula $V = 4/3\pi r^3$. The volume ratio of NLB to oocyte was then calculated based on the cube of the radius ratio. M16 medium (Sigma-Aldrich,

M7292) supplemented with 5 μmol/L milrinone was used for oocyte culture at the GV stage. For *in vitro* maturation, oocytes were cultured in M16 medium without milrinone. To obtain metaphase II (MII) oocytes *in vivo*, 3-week-old female mice were superovulated with 5 IU of human chorionic gonadotropin (hCG) at 16–20 h after PMSG injection. For the *in vitro* culture of early embryos, zygotes were collected from the oviducts of female mice at 16–20 h following hCG injection and mating with WT adult male mice, and were cultured in KSOM medium (AiBei, M1430).

2.5. Immunofluorescence

Oocytes, embryos, and cultured cells were fixed with 4% paraformaldehyde (PFA) dissolved in phosphate buffered saline (PBS) for 30 min at room temperature (RT), followed by permeabilization with membrane penetration solution (MPS) (0.3% Triton X-100 dissolved in PBS) for 30 min at RT. Samples were then blocked with blocking buffer (1% BSA, 0.1% Tween-20, 0.1% Triton X-100 in PBS) and incubated with the primary antibody (details provided in Table S2 online). Subsequently, samples were washed with washing buffer (0.1% Tween-20, 0.1% Triton X-100 in PBS) and incubated with fluorescence-labelled secondary antibody and DAPI at RT for 30 min (details of the secondary antibodies provided in Table S3 online). For CYTO staining, cells were incubated with 5 μ mol/L CYTO for 15 min at RT following the blocking step. Immunofluorescence images were captured using the Zeiss LSM880 confocal laser scanning microscope at the focal plane where fluorescence signals were most prominent and clear. To quantify fluorescence intensity within cell nuclei, the nuclear regions were delineated based on signal distribution using ImageJ. Mean pixel gray values were then measured within these defined regions. Similarly, for quantifying fluorescence in nucleoli or NLBs, ImageJ was used to outline these regions and measure the mean pixel gray values. For whole oocyte or embryo fluorescence analysis, ImageI was utilized to define the boundaries of the oocytes or embryos, and the mean pixel gray values were measured for these regions. Additionally, to analyze the fluorescence signal in the cytoplasm, three randomly selected circular regions of equal size were chosen in the cytoplasm of each oocyte to calculate mean pixel gray values, providing a representative measure of the cytoplasmic fluorescence signal.

2.6. DNase/RNase digestion for fixed cells

After fixation with 4% PFA and permeabilization with MPS, cells were rinsed three times with PBS. Cellular DNA was then digested with 0.05 U/ μ L DNase I (Beyotime, D7073) at 37 °C for 3 h. For RNA digestion, cells were treated with 0.25 mg/mL RNase A at 37 °C for 1.5 h.

2.7. Purification of BG4 and fluorescence imaging of G4s

The pSANG10-3F-BG4 plasmid (Addgene, 55756) was transformed into BL21 (DE3) *E. coli*, and a monoclonal strain was cultured in 2×YT medium supplemented with kanamycin (10 μ g/mL) at 30 °C with shaking at 220 rpm overnight. The bacterial culture was inoculated into 1 L of 2×YT medium (containing 50 μ g/mL kanamycin) at a dilution ratio of 1:100 for large-scale amplification. Upon reaching an $A_{600\text{nm}}$ of 0.6, 0.5 mmol/L IPTG was added to induce protein expression, and the culture was continued at 18 °C with shaking at 220 rpm for 16 h. Bacteria were harvested by centrifugation at 4 °C, 10,000 × g for 10 min. Protein purification was performed using BeyoGold^{IM} His-tag Purification Resin (Beyotime, P2226) according to the manufacturer's instructions. Aliquots of the BG4 antibody were stored at 4 °C for short-term use. For the fluorescence labelling of G4 structures, samples

were incubated with BG4 antibody (0.4 mg/mL) at 4 °C overnight, followed by anti-Flag antibody (Beyotime, AF0036), and fluorescence-labelled secondary antibody at RT for 1–2 h.

2.8. Chromosome spreading and immunofluorescence

Oocytes or early embryos were removed from the zona pellucida and pretreated with 1% fetal bovine serum in double-distilled water (ddH $_2$ O) for 1 min. A thin layer of ice-cold fixative (1% PFA, 0.2% Triton X-100, 3 mmol/L DDT, dissolved in H $_2$ O, pH 9.2) was applied to an adhesive slide with a pre-drawn rectangle in crayon to confine the fixative to a specific area. Each oocyte or embryo was carefully transferred to the fixative and placed in a humidified chamber overnight. For immunofluorescence, slides were washed with PBS for 10 min, blocked with blocking buffer for 30 min, and incubated with primary antibodies at 4 °C overnight. Following a PBS rinse, slides were incubated with secondary antibodies and DAPI.

2.9. Immunohistochemistry (IHC) and H&E staining

Mouse ovaries were fixed with 10% formaldehyde at 4 °C overnight, followed by dehydration in a graded ethanol series (50% to 100%). Subsequently, samples were immersed in xylene for 5-10 min and then embedded in molten paraffin. Paraffinembedded samples were sectioned into 5-7 µm thick slices. Deparaffinization and rehydration were performed by sequential immersion in xylene, ethanol and ddH₂O. For IHC staining, samples were pretreated with 3% hydrogen peroxide for 10 min, followed by 10 mmol/L citrate at 95 °C for 15 min. Samples were blocked with goat serum (ZSGB-BIO, ZLI-9056) for 1 h and then incubated with anti-DHX36 antibody (Abcam, ab70269) at 4 °C overnight, followed by HRP-labelled secondary antibody at RT for 1 h (Table S3 online). The Vectastain Elite ABC Kit (VectorLabs, PK-6100) and the DAB Substrate Kit (VectorLabs, SK-4100) were used for the chromogenic reaction. For H&E staining, samples were deparaffinized, rehydrated, stained with hematoxylin and eosin, and mounted with neutral resin.

2.10. Fluorescence in situ hybridization (FISH)

A 20×SSC stock solution was prepared in advance (3 mol/L NaCl, 0.3 mol/L sodium citrate dissolved in RNase-free H₂O). Oocytes were fixed with 4% PFA for 30 min at RT and permeabilized with 70% ethanol at 4 °C for 1 h. Subsequently, oocytes were washed with WR buffer (2×SSC, 10% formamide dissolved in RNase-free H₂O) and then incubated with HR buffer (2×SSC, 10% dextran sulfate, 10% formamide dissolved in RNase-free H2O) containing 1 μmol/L probe at 37 °C overnight. The probes used were: Cy3-labelled 18S-ITS1 (5'-Cy3-TCCTCCACAGTCTCCCGTTTAAT GATCCTT-3'); Alexa Fluor 488-labelled ITS2-28S (5'-Alexa Fluor 488-ATCTGAGGTCGCGGTCAGAAAGGGGGGACA-3'); Alexa Fluor 488-labelled 5' ETS (5'-Alexa Fluor 488-ATCGGGAGAAACAAGCGA GATAGGAATGTCTTA-3'). Afterward, oocytes were washed with WR buffer at 37 °C for 15 min and then stained with Hoechst 33342 at RT for 5 min. Finally, samples were mounted with an anti-quenching reagent and imaged using the Zeiss LSM880 confocal microscope.

2.11. Western blot

150–200 oocytes were lysed with 20 μL 2×loading buffer (25 mmol/L Tris-HCl [pH 6.8], 10% glycerol, 1% SDS, 0.04% bromophenol blue, 10% β -ME) and heated at 95 °C for 5 min. Samples were subjected to SDS-PAGE using the Bio-Rad protein electrophoresis system. Following electrophoresis, proteins were

transferred onto a polyvinylidene fluoride (PVDF) membrane. The membrane was blocked with 5% non-fat milk in TBS-T (0.1% Tween-20) for 30 min and then incubated with primary antibodies (Table S2 online) at 4 °C overnight. After washing the membrane with TBS-T three times, it was incubated with horseradish peroxidase-labelled secondary antibodies (Table S3 online) that were diluted in 5% non-fat milk. After additional washes, protein expression was visualized using WESTAR SUPERNOVA peroxide solution (Cyanagen, XLS3,0100).

2.12. Real-time quantitative PCR (RT-qPCR)

10 oocytes or early embryos were collected and subjected to reverse transcription with random primers using PrimeScript II Reverse Transcriptase (TaKaRa, 2690B) according to the manufacturer's protocol. qPCR was performed using Power SYBR Green PCR Master Mix (ABI, 4368708) with the primers listed in Table S4 (online). Relative RNA level was determined by comparing the Ct values of target genes with those of *Gapdh* or *Pgk1* as reference gene.

2.13. Streptavidin pull-down assay

The experiment was performed based on the previously reported method [22]. Mouse ovaries were lysed with 2 mL cytoplasmic lysis buffer (25 mmol/L HEPES [pH 7.9], 5 mmol/L KCl, 0.5 mmol/L MgCl₂, 0.05% NP-40, 0.1 mmol/L PMSF) on ice for 5 min. Following centrifugation at 4 °C, 2500 × g for 5 min, 2 mL nuclear lysis buffer (25 mmol/L HEPES [pH 7.9], 10% sucrose, 350 mmol/L NaCl, 0.01% NP-40, 0.1 mmol/L PMSF) was added to the pellet. The mixture was vortexed for 30 s and passed through a 20-gauge needle. Following centrifugation at 4 °C, $20,000 \times g$ for 10 min, the supernatant of the nuclear lysate was combined with the cytoplasmic lysate. The PQS (ITS1-Q1: 5' Biotin-AGGAG GGGTGGGTCGGTCTGGGTCCG-3') and the mutant (ITS1-Q1-Mut: 5' Biotin- AGGAGCCGTGCGTGCGTCTGCGTCCG-3') were diluted in binding buffer (50 mmol/L Tris-HCl [pH 7.8], 100 mmol/L KCl, 10 mmol/L NaCl, 3 mmol/L MgCl₂, 70 mmol/L glycine, and 10% glycerol) to a final concentration of 250 nmol/L. Afterwards, 500 µL lysate was mixed with 250 µL binding buffer and rotated at RT for 30 min. Then, 20 μL streptavidin-coated magnetic beads (Beyotime, P2151) were added to the mixture and incubated for an additional 30 min. Following incubation, a 20 μ L aliquot was collected as an input control. The magnetic beads were washed with RIPA buffer (50 mmol/L Tris-HCl [pH7.8], 150 mmol/L NaCl, 2 mmol/L EDTA, 1% NP-40, 0.5% sodium deoxycholate, 0.1% SDS) and then lysed with 2×loading buffer for western blot analysis.

2.14. RNA immunoprecipitation followed by qPCR (RIP-qPCR)

HEK293T cells cultured in 10 cm dishes were transfected with 10 µg pDEST-Flag, pRK5-Flag-Dhx36 or pRK5-Flag-Dhx36 $^{\triangle RSM}$ for 48 h. Cell pellets were lysed with 3 mL polysome lysis buffer (10 mmol/L HEPES [pH 7.0], 100 mmol/L KCl, 5 mmol/L MgCl₂, 0.5% NP40, 1 mmol/L DTT, 100 U/mL RNase inhibitor (RRI), 400 µmol/L VRc, protease inhibitor cocktail) at 4 °C for 15 min. After centrifugation at 4 °C, 12,000 × g for 15 min, 1 mL of the supernatants were incubated with 6 µg RNA purified from mouse ovary at 37 °C for 1 h. A 100 µL aliquot of supernatant was collected, and RNA was purified as an input control. Anti-Flag M2 Affinity Gel (Sigma, A2220) was pre-washed with NT2 buffer (50 mmol/L Tris-HCl [pH 7.4], 150 mmol/L NaCl, 1 mmol/L MgCl₂, 0.1% NP-40) for five times and incubated with the lysate mixture at 4 °C for 4 h. Following incubation, the anti-Flag gel was washed

with NT2 buffer for five times. The RNA was then purified using RNeasy Mini Kits (QIAGEN, 74106) and subjected to RT-qPCR.

2.15. RNA-seq and data analysis

10 oocytes or zygotes were washed three times with 0.2% (w/v) BSA in PBS and then collected. Each sample was supplemented with an equal amount of external RNA controls consortium (ERCC) spike-in. Library construction was performed using the established Smart-seq2 protocol [23]. Libraries were sequenced on Illumina NovaSeq 6000 platform with paired-end 150 bp reads. For data analysis, adaptor sequences were removed using Trim Galore, and quality control was carried out using the FastQC. Sequences were aligned to the mouse genome (mm10) using Hisat2 and Samtools. Raw counts were quantified using FeatureCounts. Differential expression analysis was conducted using DESeq2.

2.16. ATAC-seq and data analysis

100 oocytes were removed from zona pellucida, washed three times with 0.2% (w/v) BSA in PBS, and then collected. ATAC-seq was performed using the High-Sensitivity Open Chromatin Profile Kit 2.0 (for Illumina®) (Novoprotein, N248) according to the manufacturer's instructions. DNA fragments were purified using Tagment DNA Extract Beads (Novoprotein, N245) and amplified for 16 cycles. The final DNA products were purified with DNA Clean Beads (Novoprotein, N240). Libraries were sequenced on Illumina NovaSeq 6000 platform with paired-end 150 bp reads. For data analysis, adaptor removal and quality control were performed using the Trim Galore and FastQC. Sequence alignment to the mouse genome (mm10) was achieved using Bowtie2 and Samtools. Duplicate fragments were removed using Sambamba, and mitochondrial repeats were excluded using Samtools. Peak calling was performed using MACS. Peak enrichment and correlation were visualized using the deepTools. Peaks were annotated using R packages (ClusterProfiler, ChIPseeker, and GenomicFeatures). Motif enrichment was performed using STREME. Mouse assemblies mm10 supplemented with rDNA sequences [24] were used for rDNA alignment. Chromatin accessibility at transcription start sites (TSS) or rDNA was visualized using the IGV.

2.17. Female mice fertility test

The 6-week-old *Dhx36^{fl/fl}*; *Zp3-Cre* and *Dhx36^{fl/fl}* female mice from the same litters were mated with adult WT males. The litter and pup number were recorded for each female during the 6-month mating period.

2.18. Fluorescence spectra of CYTO

Putative G-quadruplex sequences (PQS) were predicted using QGRS Mapper [25]. Fluorescence spectra of CYTO were measured following the previously reported method [10]. Briefly, 2 μ mol/L PQS was mixed with 5 μ mol/L CYTO in reaction buffer (10 mmol/L Tris-HCl, 60 mmol/L KCl). Under the excitation wavelength at 527 nm, fluorescence spectra ranging from 550–800 nm were recorded using the multi-scan spectrophotometer.

2.19. OPP staining for translation activity detection

Translation activity was detected using the Click-iT OPP Alexa Fluor Protein Synthesis Assay Kit (Invitrogen, C10456). Briefly, oocytes, or late 2-cells were incubated with OPP reagent at 37 °C for 1 h. Afterward, oocytes were washed with M2 medium (Sigma, M7167) for 10 min, and then fixed with 4% PFA and permeabilized

with MPS. Fluorescent labeling of nascent peptides was performed according to the manufacturer's instructions.

2.20. EU staining for transcription activity detection

Transcription activity was detected using the Click-iT RNA Imaging Kits (Invitrogen, C10329). Briefly, GO, zygotes (collected at 25 h post-hCG), or late 2-cells (collected at 46 h post-hCG) were incubated with 1 mmol/L 5-ethynyl uridine (EU) in M2 medium at 37 °C for 1–2 h. Subsequently, they were washed with M2 medium for 10 min and then fixed with 4% PFA and permeabilized with MPS. Fluorescent labelling of nascent RNA was performed according to the manufacturer's instructions.

2.21. Transmission electron microscopy (TEM) and ribosome number quantification

Follicles were extracted from mouse ovaries and fixed with 2.5% glutaraldehyde at 4 °C overnight. After being rinsed with PBS, samples were fixed with 1% buffered osmium tetroxide for 1 h. Samples were washed with ddH₂O, and stained with 2% uranyl acetate for 30 min. Subsequently, samples were dehydrated using a graded series of ethanol (50%, 70%, 90%, and 100%) for 15 min at each step. Samples were then incubated with propylene. Following this, samples were embedded with an embedding medium. Sections were cut at 90 nm and placed on bar grids. The contrast was achieved using 3% uranyl acetate and Sato's lead stain. Ribosome quantification was performed following the reported methodology [26]. In this approach, ribosomes were identified based on their size (20-30 nm diameter) and characteristic morphology. Several defined square regions of interest (ROIs), each with sides measuring 220 nm in length, were selected within the cytoplasm of the oocytes. Ribosome counts were then quantified within these ROIs.

2.22. Ribosome profiling with sucrose gradient centrifugation

The MOSE cells were cultured in 10 cm dishes and treated with either DMSO or 50 nmol/L CYTO for 24 h. Afterward, the cells were incubated with DMEM containing 100 µg/mL CHX for 15 min and then washed with PBS supplemented with 100 µg/mL CHX. The cell pellets were collected and lysed with lysis buffer (25 mmol/L Tris-HCl [pH 7.4], 100 mmol/L NaCl, 5 mmol/L MgCl₂, 100 mmol/ L KCl, 1% Triton X-100, 100 µg/mL CHX, protease inhibitor cocktail, 100 U/mL RRI) on ice for 30 min. After centrifugation at $13,000 \times g$ at 4 °C for 10 min, the supernatant was collected. The lysates were then loaded onto a centrifugation tube (Beckman, 344057) containing 5 mL sucrose density gradients (10%-50%) dissolved in polysome buffer (25 mmol/L Tris-HCl [pH 7.4], 100 mmol/L NaCl, 5 mmol/L MgCl₂, 100 mmol/L KCl). The samples were centrifuged at 40,000 rpm with the MLS-50 rotor at 4 °C for 2 h. Post centrifugation, gradients were fractioned manually into 200 µL fractions, and the absorbance at 280 nm was recorded using the multiscan spectrophotometer.

2.23. In vitro transcription and microinjection

The *Dhx36* and *Dhx36*△*RSM* were cloned into the pRK5-derived expression vector and fused with a C-terminal EGFP to generate the pRK5-Dhx36-Egfp and pRK5-Dhx36△RSM-Egfp plasmids. The pRK5-Dhx36-Egfp and pRK5-Dhx36△RSM-Egfp plasmids were linearized and the *in vitro* transcription was performed using the SP6 mMEGAshortscriptTM High Yield Transcription Kit (Invitrogen, AM1340) according to the manufacturer's instructions. Polyadenylation was performed using poly (A) Tailing Kit (Invitrogen,

AM1350). Each FGO received an injection of 7–8 pL mRNA at a concentration of 1000 ng/μL. Microinjection was performed using the Eppendorf FemtoJet 4i system. For fluorescence imaging of FGO, oocytes were treated with 1% Triton X-100 in PBS for 1 min, followed by fixation with 4% PFA.

2.24. Statistical analysis

Each experiment was performed with a minimum of three independent repetitions to ensure the robustness and reproducibility of our findings. Data are presented as means \pm standard error of the mean (SEM) to indicate variability within the data. To assess the significance of differences between experimental groups, we utilized unpaired two-tailed t-tests or two-way ANOVA. Statistical significance was defined as follows: P < 0.05 (*), P < 0.01 (**), P < 0.001 (***), and P < 0.0001 (****). All statistical analyses were conducted using GraphPad Prism 9, and results were considered statistically significant when the P value was below 0.05.

3. Results

3.1. Maternal loss of DHX36 causes dysfunction in hormone response and ovulation in mice

DHX36 is highly expressed in mouse ovary compared to other tissues (Fig. 1a). Immunohistology revealed high DHX36 expression in the nuclei of mouse oocytes and granulosa cells, with prominent nucleolar localization observed in oocytes from secondary to antral follicles (Fig. 1b). The mRNA level of *Dhx36* is dynamic during oocyte growth and early embryo development (Fig. 1c). As shown in Western blot analysis using equal numbers of oocytes or zygotes, the protein level of DHX36 decreases during oocyte maturation from the GV to the MII stage and increases after fertilization (Fig. 1d).

To investigate the physiological function of DHX36, the conditional knockout (CKO) mouse model was constructed by generating the Dhx36^{fl/fl}; Zp3-Cre female mice, with the second exon of Dhx36 knocked out (Fig. 1e). The gene sequence of Dhx36 comprises 25 exons. Its coding region spans 3006 bp and encodes 1001 amino acids. However, in our knockout strategy, the removal of the second exon of *Dhx36* resulted in a premature stop codon occurring within the third exon, leaving only 234 bp from the initiation codon to the premature stop codon, preventing the translation of the full-length DHX36 protein. Successful knockout was confirmed at both mRNA and protein levels (Fig. 1f, g). The CKO mice were completely infertile during the 6-month mating period (Fig. 1h). No significant differences were observed between the wild-type (WT) and CKO ovaries from mice aged 8 or 10 weeks, regarding size (Fig. 1i), weight (Fig. 1j), or histology (Fig. 1k). However, we found that ovulation was dramatically reduced with age, resulting in no oocytes being retrieved from the oviducts after superovulation treatment when CKO mice reached 4-5 weeks of age (Fig. 11). Dilated follicles and expanding ampullae of fallopian tube were barely observed in CKO mice at 4-5 weeks old (Fig. 1m). Further H&E staining results indicate a significant reduction in the number of granulosa cell layers surrounding the oocytes within antral follicles in CKO ovaries compared to WT at PMSG-44 h (Fig. 1n). At hCG-8 h, most cumulus-oocyte complexes (COCs) in WT antral follicles exhibit substantial cumulus expansion, and the oocytes have resumed meiosis. In contrast, the cumulus expansion in the CKO group is inadequate, with granulosa cells still closely surrounding the oocytes, which remain at the GV stage (Fig. 1n). By hCG-16 h, the majority of antral follicles have undergone ovulation and formed corpora lutea (CL); however, CKO

oocytes in antral follicles fail to ovulate and the granulosa cells show complete detachment from the oocytes along with signs of oocyte fragmentation (Fig. 1n). Taken together, these results suggest that maternal DHX36 in mouse oocyte plays a critical role in maintaining female fertility.

3.2. DHX36 deficiency disrupts chromatin configuration and chromatin accessibility in mouse GV oocytes

Quantitative analysis of ZP thickness using bright-field imaging and phalloidin staining revealed that the ZP in CKO GV oocytes is thinner compared to WT oocytes (Fig. S1a–c online). Additionally, we found that the NLBs in CKO oocytes were abnormally larger than those in the WT group (Fig. 2a, b). During the NSN-to-SN transition, chromatin condenses to form a heterochromatin ring, also known as a "karyosphere". CKO oocytes exhibited larger karyospheres and a reduced diameter of DAPI-dense heterochromatin foci (Fig. 2c, d). Moreover, CKO oocytes showed lower expression level of histone modifications, including H3K4me3, H3K27me3 and H3K9me3 (Fig. 2e, f and Fig. S1d–h online). Consequently, the HP1 α associated with H3K9me3 and heterochromatin foci [27,28], shows a dispersed distribution across the chromatin in CKO GV oocytes (Fig. 2g, h).

ATAC-seg was performed on GO and FGO from WT and CKO mice, with high correlation between replicates and similar genomic proportion between groups (Fig. S2a, b online). Among shared peaks in GO of WT and CKO groups, peak gain and loss in CKO GO account for nearly half each in CKO GO (Fig. 2i), while peak loss accounts for nearly 70% in CKO FGO (Fig. 2j). Chromatin accessibility at transcription start sites (TSS) decreases from GO to FGO, showing negligible differences between WT and CKO GO but exhibiting a significant decline in CKO FGO (Fig. 2k). Chromatin accessibility at rDNA regions (from 5' ETS to 3' ETS) significantly decreases in CKO GO but shows negligible difference in FGO (Fig. 21). Unique motif enriched in the CKO groups is highly consistent with the reported G4 motif detected by G4 ChIP-seq [29] (Fig. 2m). Collectively, these results suggest that DHX36 is essential for maintaining chromatin configuration and accessibility.

3.3. DHX36 deficiency impedes meiosis progression and embryo development

During *in vitro* maturation (IVM) culture, CKO oocytes exhibit a dramatically reduced rate of germinal vesicle breakdown (GVBD) and polar body (PB) extrusion (Fig. 3a-c). WEE2, an inhibitory factor of Maturation-Promoting Factor (MPF), along with CDK1 and its phosphatase CDC25B, is downregulated in the CKO group (Fig. 3d). During IVM culture, CKO oocytes display inadequate levels of p-ERK1/2 and accumulated CPEB1, both of which are crucial for translation activation during meiosis resumption [30,31] (Fig. 3e).

Superovulation was conducted, and only 73% of ovulated CKO oocytes exhibited polar bodies, while the rest were either arrested or fragmented (Fig. 3f). Among the CKO oocytes with polar bodies, significantly larger polar bodies were observed (Fig. 3g, h). Abnormal spindles with increased sizes were frequently noted in the CKO group (Fig. 3i–k), and approximately half of the CKO oocytes displayed chromosome aneuploidy (Fig. 3l). At 26 h post hCG, the pronucleus formation rate was significantly decreased in the CKO group compared to the WT (Fig. 3m). Furthermore, over 80% of early embryos eventually arrested at the zygote or 2-cell stage or degenerated during *in vitro* culture (Fig. 3n, o). Taken together, these findings underscore the critical role of DHX36 in meiosis resumption and early embryo development.

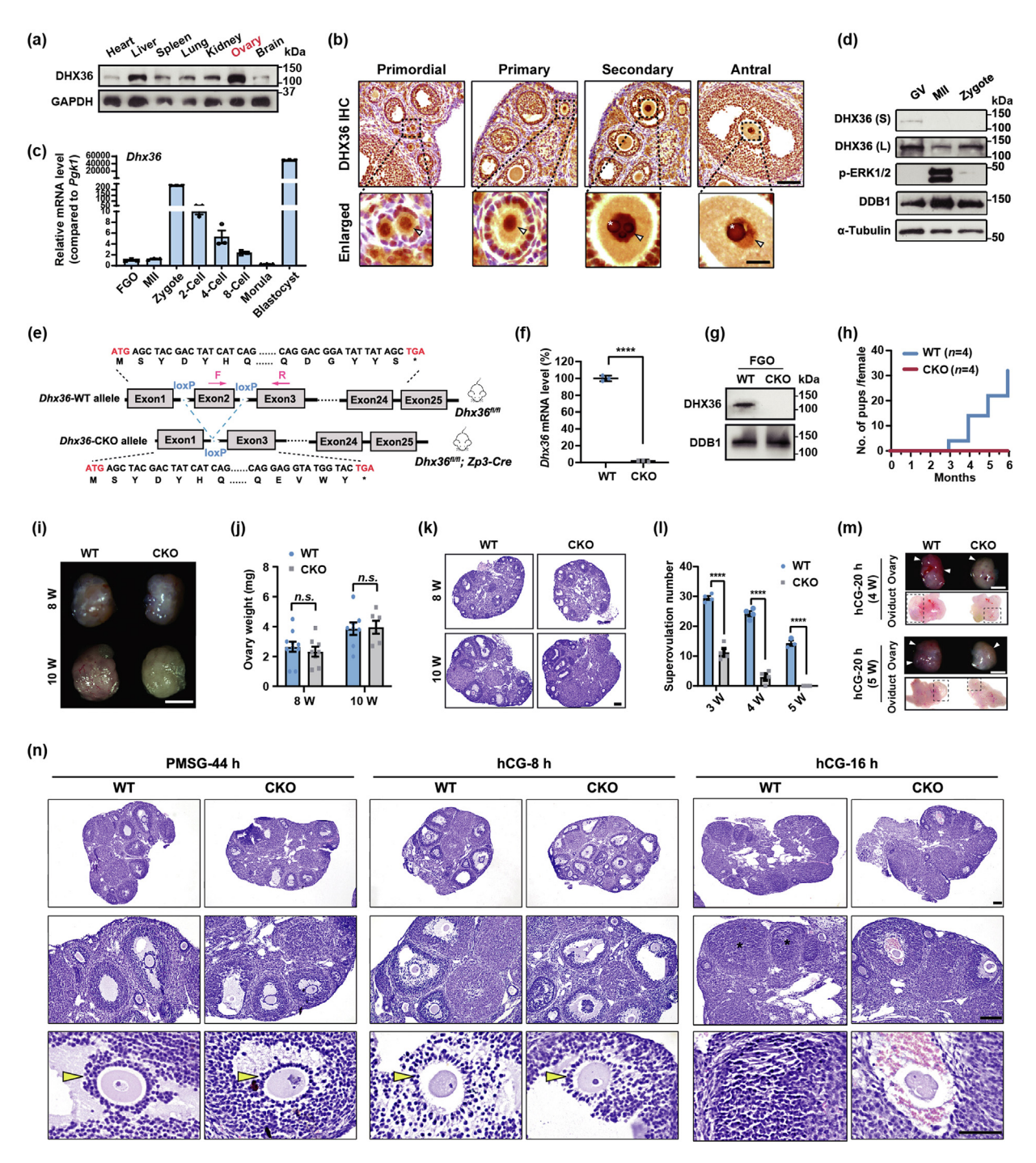


Fig. 1. Maternal DHX36 is indispensable for maintaining female mice fertility. (a) Western blot analysis of DHX36 protein level in various mouse organs. (b) IHC images depicting DHX36 localization in different follicles of mouse ovaries. Triangles indicate oocyte nuclei, and asterisks denote nucleoli. Scale bar, 100 μm and 25 μm (Enlarged). (c) RT-qPCR analysis presenting relative Dhx36 mRNA level compared to the reference gene Pgk1 [49] at different developmental stages. (d) Western blot analysis of DHX36 protein expression in GV, MII oocytes, and zygotes, with 150 samples per group. DHX36 protein was exposed for short (S) and long (L) durations. DDB1 was used as a loading control, while p-ERK1/2 serves as an indicator of different developmental stages. (e) Gene editing strategy for oocyte-specific knockout of Dhx36. Pink arrows indicate the forward (F) and reverse (R) primers used for RT-qPCR. (f) RT-qPCR analysis of Dhx36 mRNA level in WT and CKO FGO. (g) Western blot analysis of DHX36 protein expression in WT and CKO FGO. (h) Average number of pups delivered by WT and CKO mice during the 6-month mating period. (i) Images displaying ovarian morphology of WT and CKO mice at 8 and 10 weeks old. Scale bar, 1 mm. (j) Ovary weight of WT and CKO mice at 8 and 10 weeks old. (k) H&E staining images showing the ovarian histology in WT and CKO mice at 8 and 10 weeks old. Scale bar, 100 μm. (l) Number of oocytes collected from WT and CKO mice aged 3–5 weeks, at 16–20 h post hCG. (m) Images showing the morphology of ovaries and oviducts from WT and CKO female mice aged 4 and 5 weeks, at 20 h post hCG. White triangles indicate ovarian follicles, and the dashed rectangles mark the ampulla of fallopian tube. Scale bar, 1 mm. (n) The H&E staining of ovaries from 5-week-old WT and CKO mice at PMSG-44 h, and hCG-8 h or hCG-16 h after PMSG injection. Yellow triangles indicate the COCs, and asterisks (*) denote the CL. Scale bar: 100 μm, 100 μm, and 50 μm (from top to bottom). Data are presented as mean \pm SEM. P v

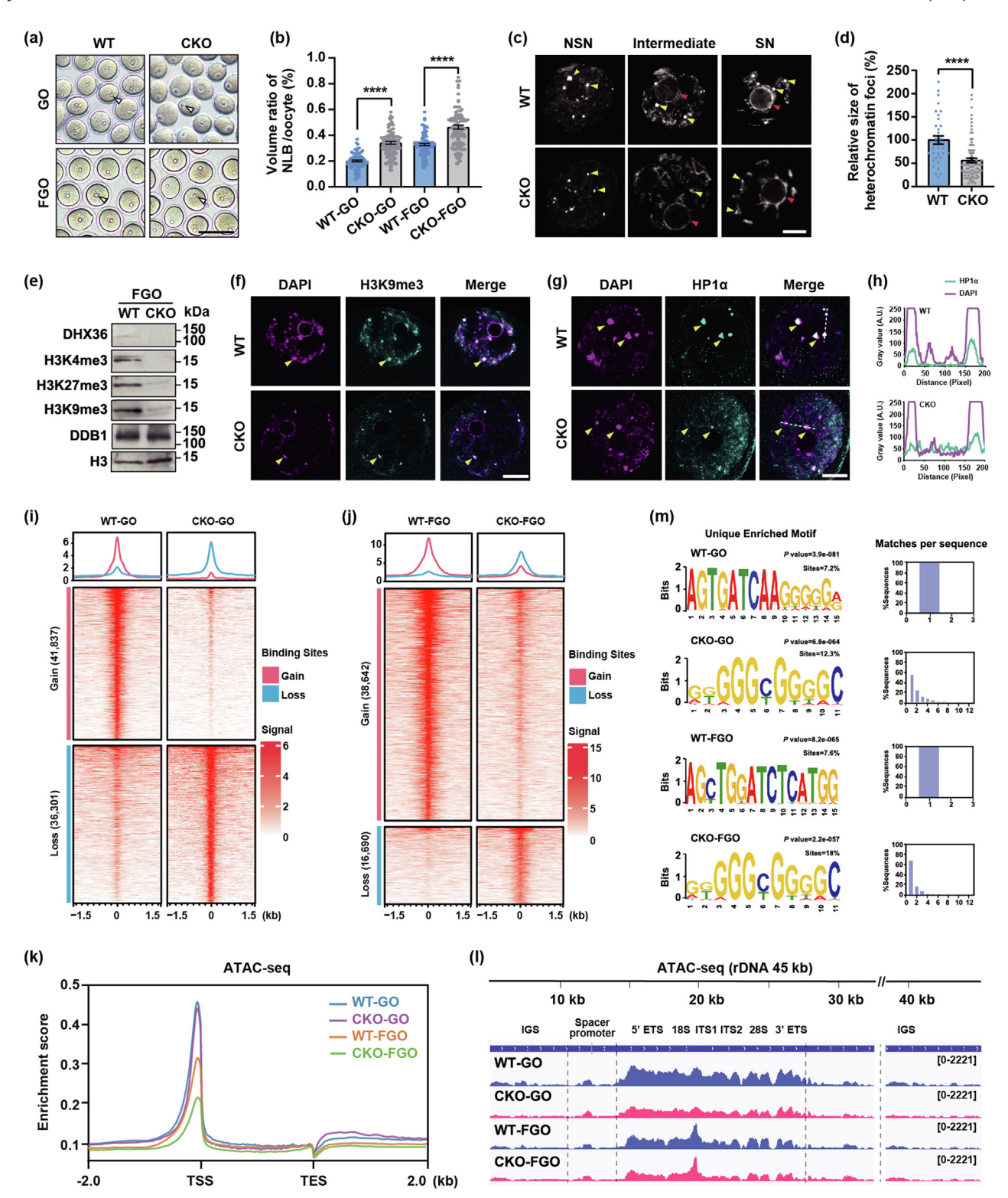


Fig. 2. DHX36 preserves chromatin accessibility in mouse GV oocytes. (a) Images showing the morphology of WT and CKO oocytes. Triangles indicate the NLBs. Scale bar, 100 μm. (b) Volume ratio of the NLB to the total oocyte volume. (c) Fluorescence images showing the chromatin in FGO stained with DAPI. Scale bar, 20 μm. Yellow triangles indicate DAPI-dense heterochromatin foci, and the red triangles denote the nucleoli or NLBs. (d) Relative size of DAPI-dense heterochromatin foci in WT and CKO FGO. (e) Western blot analysis of protein levels of H3K4me3, H3K27me3 and H3K9me3 in WT and CKO FGO. (f) Immunofluorescence images showing H3K9me3 signal across chromatin of WT and CKO FGO. Yellow triangles indicate DAPI-dense heterochromatin foci. Scale bar, 20 μm. (g) Immunofluorescence images illustrating HP1α signal across chromatin of WT and CKO FGO. Yellow triangles indicate DAPI-dense heterochromatin foci. Scale bar, 20 μm. (h) Distribution of DAPI and HP1α signal intensity along the white dashed lines shown in panel (g). (i, j) Heatmaps showing peak gain and loss in WT and CKO GO/FGO, detected by ATAC-seq. (k) General chromatin accessibility ranging from TSS to transcription end site (TES) of WT and CKO GO/FGO. (l) Chromatin accessibility of rDNA in WT and CKO GO/FGO. (m) Unique motif enriched in WT and CKO GO/FGO. Data are presented as mean ± SEM. *P* values were calculated by unpaired t-tests (b and d). *****P < 0.0001.

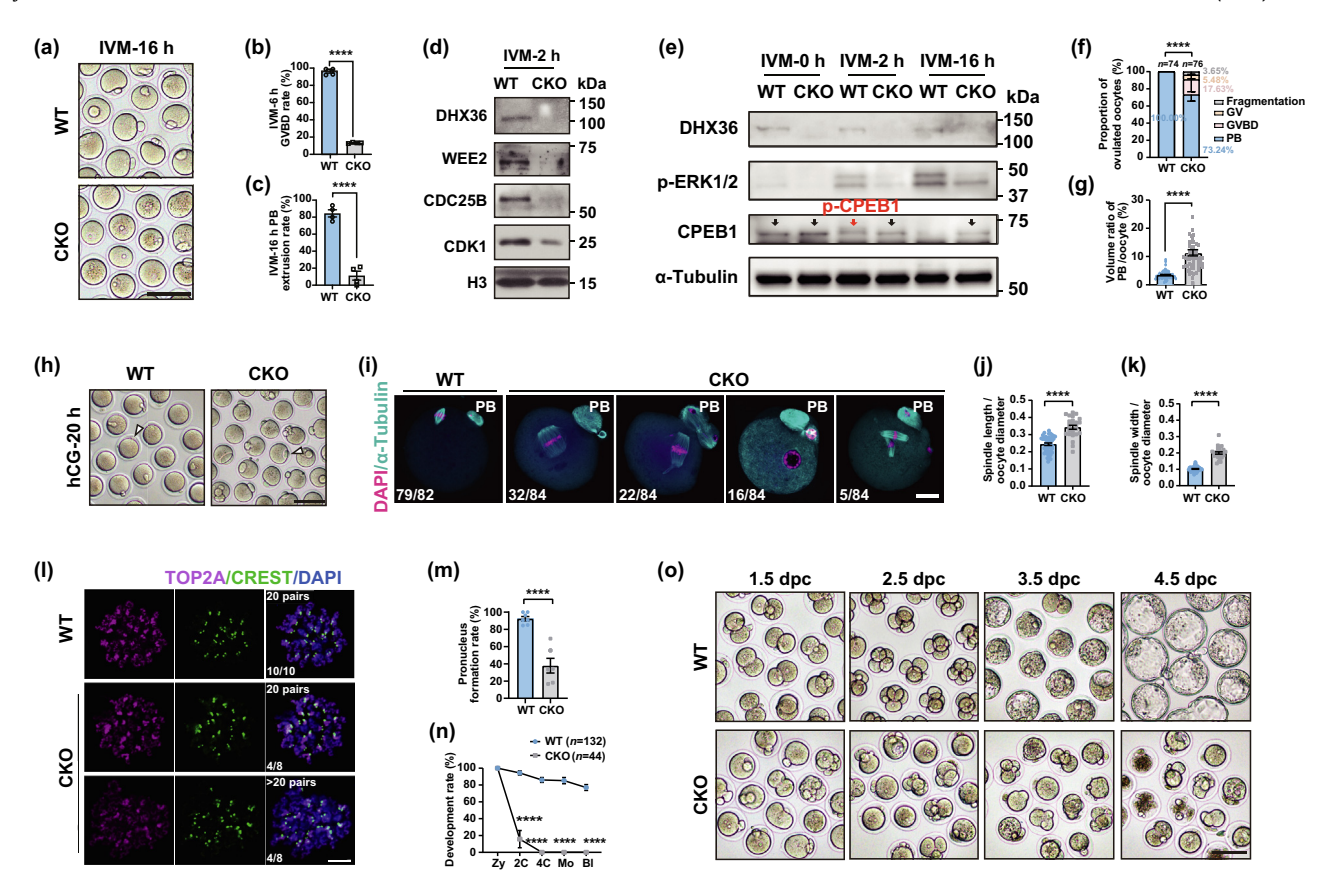


Fig. 3. DHX36 is essential for meiosis resumption and early embryo development. (a) Images showing the morphology of oocytes at IVM-16 h. Scale bar, 100 μm. (b) The GVBD rate of oocytes at IVM-6 h. (c) The polar body (PB) extrusion rate of oocytes at IVM-16 h. (d) Western blot analysis of protein levels of WEE2, CDC25B and CDK1 at IVM-2 h. (e) Western blot analysis of protein levels of CPEB1 and phosphorylated ERK1/2 (p-ERK1/2) at IVM-0 h, IVM-2 h and IVM-16 h. Black arrows indicate the CPEB1 protein, while the red arrow indicates the phosphorylated CPEB1 (p-CPEB1) with upward migration (f) Proportion of ovulated oocytes collected from the oviducts of WT and CKO mice. (g) The volume ratio of polar body to the oocyte. (h) Images showing oocytes collected at 20 h post-hCG. The triangles indicate the polar bodies. Scale bar, 100 μm. (i) Immunofluorescence of α-Tubulin in oocytes with polar bodies. Scale bar, 20 μm. (j, k) Ratio of spindle length and width to oocyte diameter. (l) Immunofluorescence of TOP2A and CREST in chromosome spreading samples. Scale bar, 5 μm. (m) Pronucleus formation rate at 26 h post-hCG. (n) Early embryo development rate. (o) Images displaying early embryos at different days post-copulation (dpc). Scale bar, 100 μm. Data are presented as mean ± SEM. Statistical analyses were performed using unpaired *t*-tests (b, c, g, j, k, m and n) or two-way ANOVA (f). ****P < 0.0001.

3.4. DHX36 deficiency disrupts the transcriptome during oocyte growth and maternal-to-zygotic transition

Poly (A) RNA-seq was performed in GO, FGO, MII and zygote (Table S5 online). The RNA quantities between WT and CKO groups were comparable at each stage (Fig. S3a online). Replicates within each group showed relatively high correlation, with significant deviation observed between WT and CKO groups at the FGO stage (Fig. 4a). A substantial number of differentially expressed genes (DEGs) were identified in CKO FGO, with 3773 up-regulated and 1851 down-regulated genes (Fig. 4b). However, the FPKM values of the up-regulated genes were generally lower than those of the down-regulated genes (Fig. 4c), and the 5-ethynyl uridine (EU) staining of FGO with NSN configuration revealed a significantly reduced transcription activity in the CKO group (Fig. 4d and Fig. S3b online). Combined analysis of RNA-seq and ATAC-seq data demonstrated generally higher chromatin accessibility at TSS in down-regulated genes compared to the up-regulated genes, and both the up- and down-regulated genes showed a slightly decreased chromatin accessibility at CKO GO and a significantly declined chromatin accessibility in CKO FGO (Fig. 4e, f). The reported poly(A) RNA-seq data [32] has revealed transcriptome alterations among early GO, late GO and FGO, with some genes gradually accumulating and others decreasing during oocyte

growth (Fig. 4g, h). We found that a significant proportion of DEGs in CKO FGO originated from the DEGs identified in CKO GO, and a large proportion of up-regulated genes in CKO FGO belonged to those requiring a decrease from early/late GO to FGO, while a large proportion of down-regulated genes in CKO FGO belonged to those requiring accumulation from early/late GO to FGO (Fig. 4i).

Maternal-to-zygotic transition (MZT) signifies the transfer of developmental control from maternal factors to the zygotic genome, involving maternal mRNA clearance and zygotic genome activation (ZGA) [33]. We found that a large proportion of DEGs in CKO MII oocytes originated from the DEGs identified in CKO FGO, and that most of the up-regulated genes in CKO MII belonged to those requiring a decrease from FGO to MII, while a significant proportion of the down-regulated genes belonged to those with an increased ratio from FGO to MII. (Fig. 4j). Similarly, a substantial proportion of DEGs in CKO zygotes was inherited from DEGs identified in CKO MII, and that a large proportion of up-regulated genes in CKO zygotes belonged to those requiring a decrease from MII to zygote, while down-regulated genes in CKO zygotes predominantly belonged to those requiring an increase from MII to zygote (Fig. 4k). The EU staining revealed significantly reduced transcription activity in CKO zygote compared to the WT (Fig. 4l, m). Collectively, these results reveal the transcriptome disturbances during oocyte growth and MZT in Dhx36-deficient oocytes.

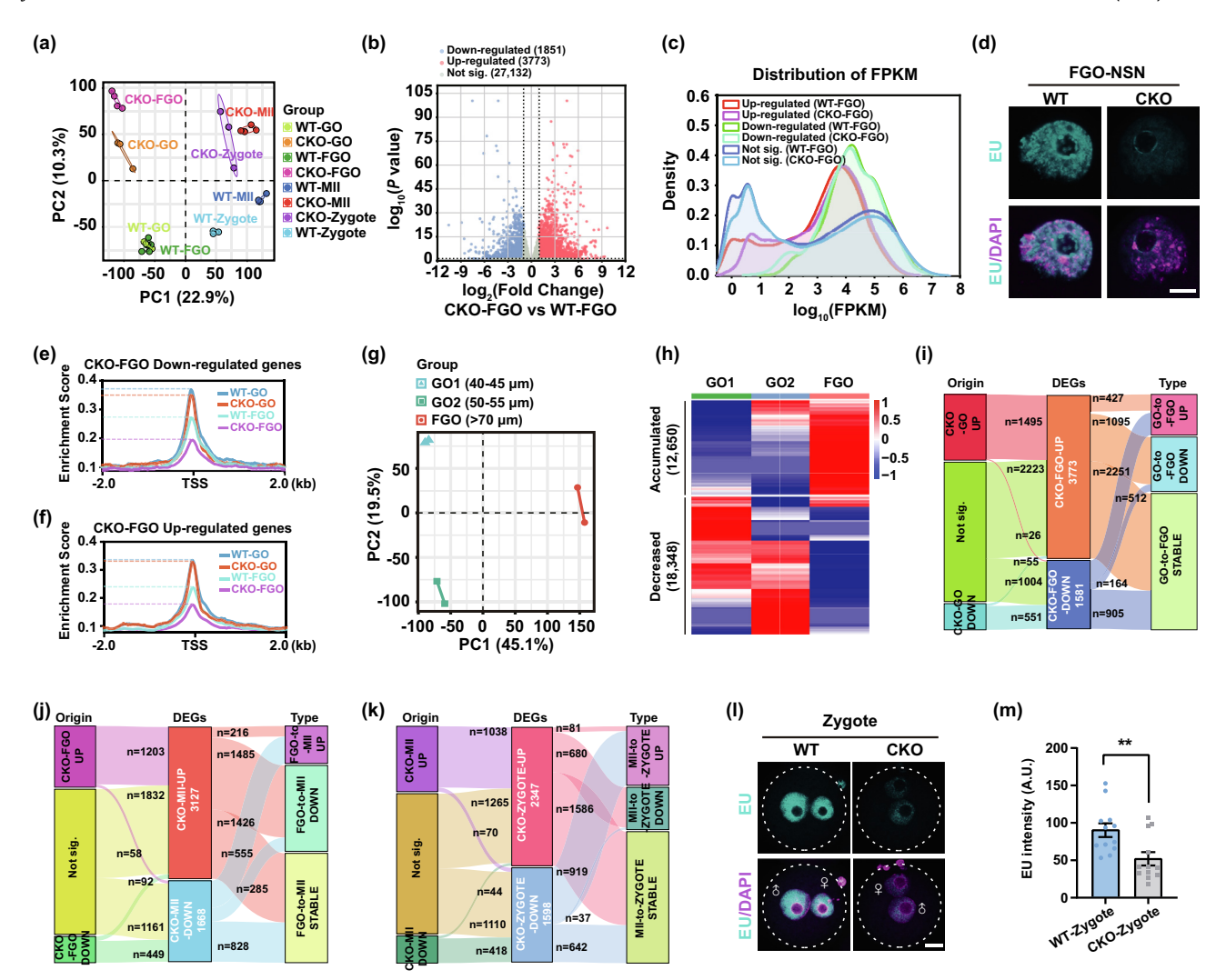


Fig. 4. The crucial role of DHX36 in preserving mRNA homeostasis. (a) Principal Component Analysis (PCA) illustrating the correlation of RNA-seq data. (b) Volcano plot depicting DEGs between WT and CKO FGO. Abbreviation: Not significant (Not sig.). (c) Distribution of FPKM values of DEGs identified in CKO FGO. (d) Fluorescence images displaying EU staining of WT and CKO FGO with NSN configuration. Scale bar, $20~\mu m$. (e) Chromatin accessibility of down-regulated genes in CKO FGO. (f) Chromatin accessibility of up-regulated genes in CKO FGO. (g) PCA showing the correlation among reported RNA-seq data of early GO (GO1), late GO (GO2) and FGO. (h) Heatmap demonstrating gene expression patterns transitioning from early GO, late GO to FGO. (i) Sankey diagram showing the origin and type of DEGs identified in CKO FGO, with origin classified by DEGs in CKO GO, and type based on DEGs between early/late GO and FGO. (j) Sankey diagram showing the origin and type of the DEGs identified in CKO MII oocytes, with origin classified by DEGs between WT and CKO FGO, and type based on DEGs between FGO and MII oocytes. (k) Sankey diagram demonstrating the origin and type of DEGs identified in CKO zygotes, with origin classified by DEGs between WT and CKO MII oocytes, and type based on DEGs between MII oocytes and zygotes. (l) Fluorescence images of EU staining in WT and CKO zygotes at 25–27 h post-hCG. Scale bar, $20~\mu m$. (m) Quantification of EU signal intensity in WT and CKO zygotes. DEGs in each stage are categorized as up-regulated [log₂Fold Change (CKO/WT) ≥ 1 , P < 0.05]. Data are presented as mean \pm SEM. Unpaired t-test was used for statistical analysis (m). **P < 0.05] or down-regulated [log₂Fold Change (CKO/WT) ≤ -1 , P < 0.05]. Data are presented as mean \pm SEM. Unpaired t-test was used for statistical analysis (m). **P < 0.05]

3.5. DHX36 deficiency inhibits the transcription and processing of prerRNA in GV oocytes

Gene Ontology analysis revealed that up-regulated genes in CKO GV oocytes were enriched in biological processes, including ribonucleoprotein complex biogenesis, negative regulation of translation, and rRNA processing (Fig. 5a). RT-qPCR analysis showed a significantly decreased level of pre-rRNA in CKO GO (Fig. 5b, c). However, CKO FGO exhibited a significantly increased pre-rRNA level along with a remarkable reduction in total rRNA (Fig. 5d). By using the FISH probe spanning the 5' ETS of pre-rRNA, we observed a significant decrease of rRNA transcription in CKO GO, with a noticeable reduction of the pre-rRNA signal in the nucleolus (Fig. 5e, g). In contrast, CKO FGO displayed a significantly increased pre-rRNA signal in the cytoplasm (Fig. 5f, h). These results indicate the obstacles involved in pre-rRNA transcription and processing in *Dhx36*-deficient oocytes.

Transmission electron microscopy (TEM) observations of GV oocytes in antral follicles revealed that the nuclei of CKO oocytes contained more pre-ribosomal particles (approximately 20 nm in diameter), while fewer ribosomes were observed in the cytoplasm of CKO oocytes (Fig. 5i, k). OPP staining demonstrated a significantly decreased translation efficiency in CKO FGO (Fig. 5j, l). Taken together, these findings suggest that DHX36 deficiency impedes oocyte growth, possibly through inhibiting mature rRNA production and ribosome biogenesis.

3.6. DHX36 deficiency enhances G4s accumulation in mouse GV oocytes

The nucleolus serves as the site for rRNA transcription, which decreases along with nucleolus-to-NLB transformation during oocyte growth (Fig. 6a). We observed a distinctly enhanced DHX36 signal at the periphery of the nucleolus/NLB in GV oocytes

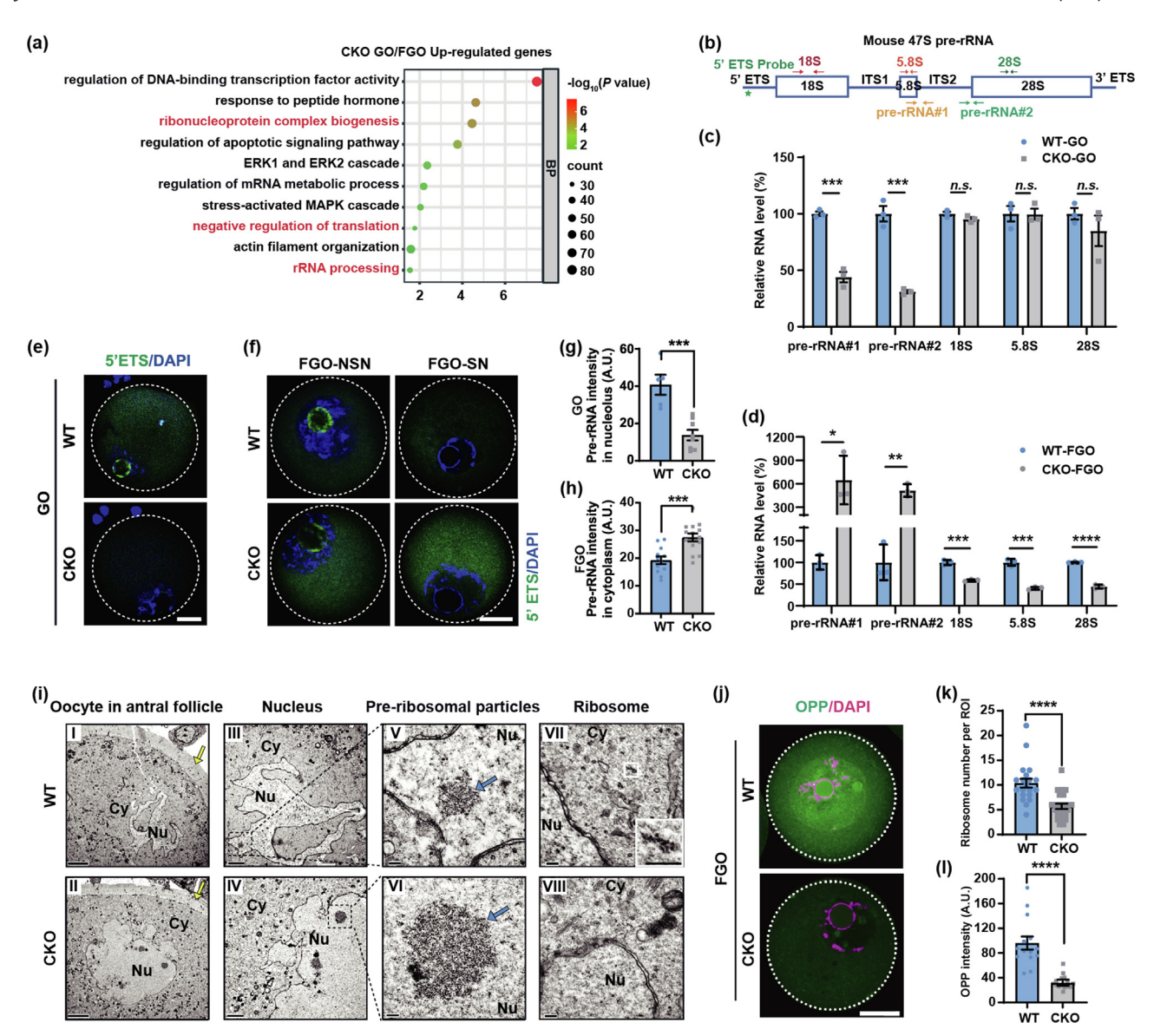
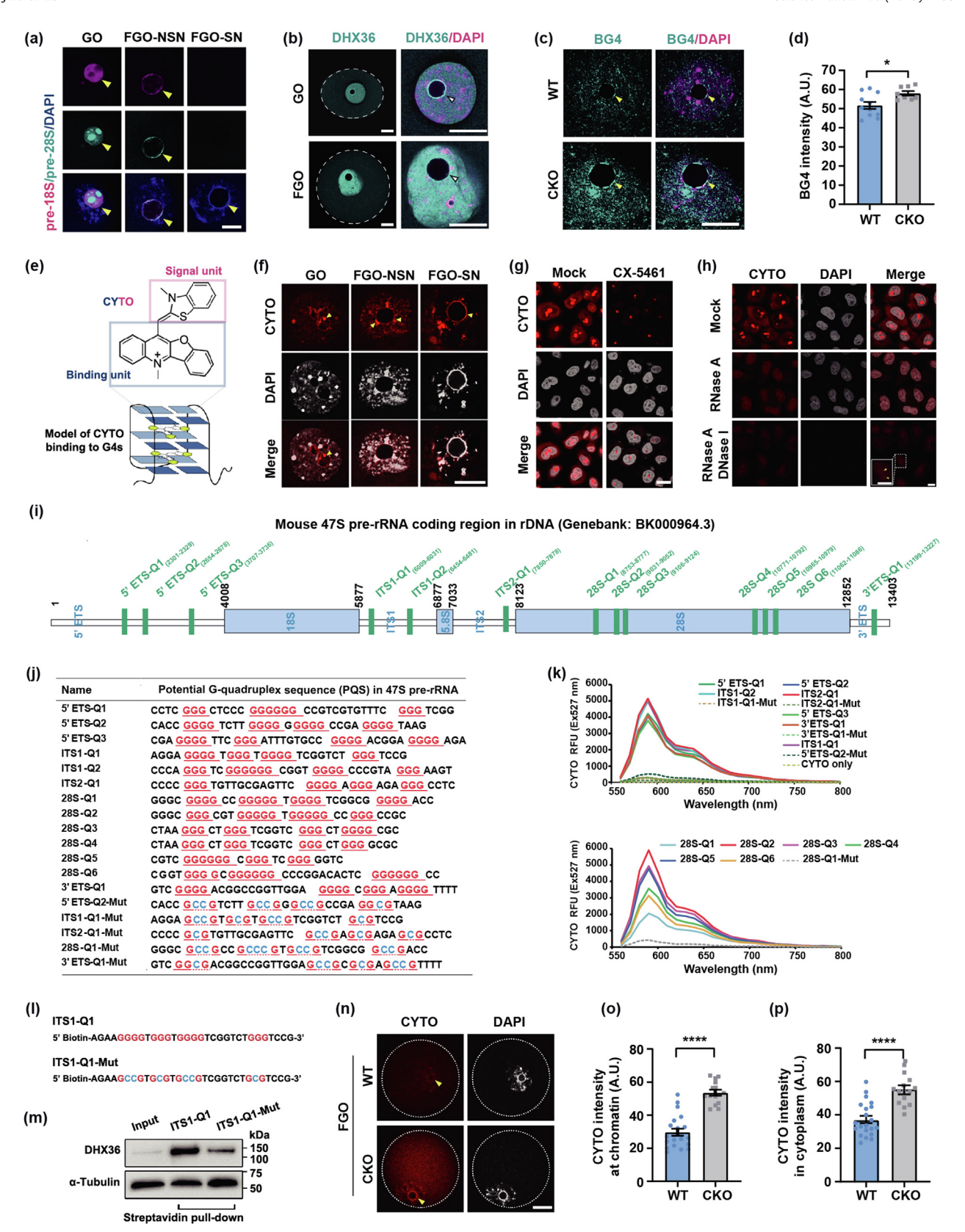


Fig. 5. DHX36 is indispensable for rRNA production and ribosome biogenesis in mouse GV oocytes. (a) Gene Ontology analysis of up-regulated genes in CKO GO/FGO. (b) Schematic representation of elements in mouse 47S pre-rRNA, indicating the location of FISH probes and qPCR primers. (c) qPCR analysis of pre-rRNA and rRNA level in WT and CKO GO. (d) qPCR analysis of pre-rRNA and total rRNA level in WT and CKO FGO. (e) FISH showing pre-rRNA (5' ETS) signal in WT and CKO GO. Scale bar, 20 μm. (f) FISH showing pre-rRNA (5' ETS) signal in WT and CKO GO. Scale bar, 20 μm. (g) Quantification of fluorescence intensity of pre-rRNA (5' ETS) in the nucleolus of WT and CKO GO. (h) Quantification of fluorescence intensity of pre-rRNA (5' ETS) in the cytoplasm of WT and CKO FGO. (i) TEM images showing the morphology of WT and CKO GV oocytes in antral follicles. Yellow arrows indicate the zona pellucida; bule arrows denote pre-ribosomal particles in the nucleus; white rectangle highlights a defined ROI within the cytoplasm. Abbreviations: Cytoplasm (Cy); Nucleus (Nu). Scale bars: 5 μm (II-II), 2 μm (III-IV), 200 nm (V-VIII). (j) OPP staining showing the translation efficiency in WT and CKO FGO. Scale bar, 20 μm. (k) Quantification of ribosome numbers per ROI. (I) Relative OPP fluorescence intensity measured in WT and CKO FGO. Data are presented as mean ± SEM. Unpaired t-tests were used for statistical analyses (c, d, g, h, k and l). P > 0.05 (n.s.), *P < 0.05, **P < 0.01, ***P < 0.001 and *****P < 0.0001.

(Fig. 6b). The G4 antibody, BG4, was successfully purified and validated by Coomassie staining, western blot and immunofluorescence (Fig. S4a–d online). The BG4 displays an enhanced signal in the nuclei of CKO GV oocytes, particularly at the periphery of the nucleoli (Fig. 6c, d). The small-molecule fluorescent G4 probe, CYTO, which binds to G4 through an end-stacking model [10] (Fig. 6e), also exhibits an enhanced signal around the nucleoli or NLBs in GV oocytes (Fig. 6f). In HeLa cells, the CYTO preferentially binds to pre-rRNA, as its main signal within the nucleolus significantly diminished after treatment with CX-5461, an RNA polymerase I inhibitor (Fig. 6g). Upon RNase A treatment, the CYTO signal shifted to the nucleoplasm and further decreased after both RNase A and DNase I treatment; notably, the signal around the nucleolus associated with the rDNA regions [34] became more

pronounced (Fig. 6h). Putative G-quadruplex sequences (PQS) mapping revealed high-scoring G4 candidates in the mouse rDNA region, some of which were located near the reported pre-rRNA cleavage sites [35] at external transcribed spacers (ETS) and internal transcribed spacers (ITS) (Fig. 6i). A strong fluorescence signal was observed when the CYTO was incubated with synthesized PQS, while minimal signal was detected when the CYTO was incubated with mutant PQS carrying G-to-C substitutions (Fig. 6j, k).

Biotin-labelled PQS, ITS1-Q1, was synthesized for incubation with ovarian lysates, followed by streptavidin pull-down and western blot. ITS1-Q1 exhibited a higher affinity for DHX36 compared to the mutant probe, ITS1-Q1-Mut (Fig. 6l, m). Furthermore, a significantly enhanced CYTO signal was observed in both chromatin and cytoplasm of CKO FGO (Fig. 6n-p). Collectively, these findings



suggest that DHX36 deficiency induces the G4s accumulation in mouse GV oocytes, which may result from its interaction with G4s on rDNA and pre-rRNA.

3.7. G4s stabilization inhibits transcription and processing of pre-rRNA in mouse GV oocytes and early embryos

Treatment with the G4 stabilizer pyridostatin (PDS) leads to a remarkable increase of CYTO signal in HeLa cells, with the signal within the nucleoli preserved despite RNase A treatment (Fig. 7a). CYTO also acts as a G4 stabilizer, as CYTO treatment induces a significant increase in BG4 signal in HeLa cells (Fig. S5a-b online). Sucrose gradient centrifugation revealed that the 60S ribosome subunit and polysomes were severely disrupted upon CYTO treatment (Fig. 7b). Additionally, an elevated pre-rRNA level was detected in GO treated with CYTO (Fig. 7c).

CYTO has a negligible influence on oocvte maturation rate (Fig. 7d), but significantly decreases the translation efficiency in MII oocytes (Fig. 7e, f). Oocytes treated with CYTO exhibited a comparable proportion of unaligned chromosomes and spindle abnormalities (Fig. 7g, h). With a limited development rate to 4-cell stage, early embryos treated with CYTO were mostly arrested at the 2-cell stage (Fig. 7i, j). This treatment resulted in inhibited transcription activity, as evidenced by reduced level of EU, phosphorylated RNA polymerase II (pS2) and H3K4me3 signal in the nucleus of late 2-cell (L2C) embryos (Fig. S6a-f online). Meanwhile, the L2C embryos in CYTO-treated group exhibited significantly decreased translation efficiency (Fig. 7k, 1) and pre-rRNA level (Fig. 7m). Moreover, pre-rRNA signal was barely detectable within the nucleoli of 4-cell embryos treated with CYTO (Fig. 7n). Taken together, these results suggest that G4 stabilization by CYTO could inhibit pre-rRNA transcription or processing in mouse oocytes and early embryos, with potential effects depending on developmental stages and specific biological events.

3.8. DHX36 promotes pre-rRNA processing in mouse oocytes

FISH of pre-rRNA revealed that rRNA transcription is silenced in zygotes and early 2-cell stages but gradually increases from L2C to blastocyst stages (Fig. 8a). CYTO primarily localizes to chromatin in zygotes and 2-cell stages, gradually translocating to nucleoli from 4-cell to blastocyst stages, spatiotemporally synchronized with the pre-rRNA transcription (Fig. 8b). Similarly, BG4 antibody exhibits a dynamic localization shift from chromatin to nucleoli during early embryo development (Fig. 8c). Moreover, DHX36 shares a similar dynamic distribution pattern with CYTO and BG4 in mouse early embryos (Fig. 8d). To investigate whether DHX36 binds to pre-rRNA through its G4-binding domain, RNA immunoprecipitation (RIP)-qPCR was conducted using eukaryotic expression of FLAG-DHX36 and FLAG-DHX36 $^{\triangle RSM}$, the latter with a deleted RHAU-specific motif (RSM) known for G4 binding (Fig. 8e, f). Overexpression of both proteins was verified by western blotting (Fig. 8g), and both showed a predominant cytoplasmic localization in HEK293T cells (Fig. 8h). Compared to the FLAG and FLAG-DHX36 $^{\triangle RSM}$, FLAG-DHX36 enriched abundant pre-rRNA (Fig. 8i).

Overexpression of DHX36-EGFP or DHX36^{ARSM}-EGFP was achieved via mRNA microinjection. DHX36-EGFP exhibited a dispersed distribution in FGO (Fig. 8j) but showed dominant chromatin localization, enhancing around the NLBs after Triton treatment (Fig. 8k). In contrast, the DHX36^{ARSM}-EGFP remained outside the nucleus after Triton treatment, showing a dispersed distribution in FGO (Fig. 8j, k). Notably, the pre-rRNA level in CKO FGO significantly decreased upon DHX36-EGFP overexpression; however, no significant change was observed with the overexpression of DHX36^{ARSM}-EGFP (Fig. 8l). Collectively, these results suggest that DHX36 directly interacts with pre-rRNA and promotes pre-rRNA processing through its capacity for G4s recognition and unwinding.

4. Discussion and conclusion

Numerous studies have established a strong association between G4 structures, G4 helicases and various cellular processes, including telomere maintenance [36], transcription regulation [37,38], chromatin accessibility [39], genomic stability [38,40], epigenetic modification [41], and DNA replication [42]. DHX36 displays diverse cellular localizations and functions, which vary by cell type or tissue [16,17,43-45]. The G4 recognition and unwinding abilities of DHX36 helicase have been elucidated through the RSM and C-terminal OB-fold domain [12]. Previous studies have mainly implicated DHX36 in transcription regulation via promoter G4 unwinding [13,16] or in the modulation of mRNA translation by resolving G4s in untranslated regions [17,22,43]. In this study, we reveal a novel function of DHX36 on rRNA biology in mouse oocytes. Our findings demonstrate that the poor developmental competence of Dhx36-deficient oocytes primarily stems from inhibited pre-rRNA transcription and processing, insufficient ribosome production, and translation activity.

The rRNA constitutes over 80% of the total cellular RNA, and previous studies have suggested G4 formation in conserved rRNA sequences [46-48]. By using the small-molecule G4 probe CYTO and G4 antibody BG4, we initially discovered abundant G4 formation in pre-rRNA in mouse oocytes and early embryos. DHX36 also preferentially binds with pre-rRNA in mouse oocytes and early embryos (Fig. 9a). This specific binding preference may depend on pre-rRNA production level and G4 formation, as DHX36 only exhibits nucleolar distribution at stages with active rRNA transcription, while showing predominant chromatin distribution at stages with silent rRNA transcription. In addition, the rRNA homeostasis and ribosome biogenesis are severely disrupted in CKO GV oocytes due to G4 accumulation in rDNA and pre-rRNA (Fig. 9b). Moreover, G4 stabilization can affect rRNA homeostasis, and in vitro G4 stabilization could result in different consequences. For instance, CYTO treatment at the GO stage with active rRNA transcription leads to pre-rRNA accumulation, while treatment at early embryo stages with low rRNA transcription level leads to



Fig. 6. DHX36 exhibits strong affinity for rDNA enriched with G-quadruplexes. (a) FISH of pre-18S and pre-28S in GO and FGO. Triangles indicate the nucleolus or NLB in the oocytes. Scale bar, 20 μm. (b) Immunofluorescence staining of DHX36 in mouse GO and FGO. Triangles indicate the nucleolus or NLB of the oocytes. Scale bar, 20 μm. (c) Fluorescence imaging of BG4 in the nucleus of WT and CKO GO. Triangles indicate the nucleoli in the oocytes. Scale bar, 10 μm. (d) Quantification of relative signal intensity of BG4 in the nucleus. (e) Molecular structure and end-stacking G4-binding model of CYTO. (f) Fluorescence imaging of CYTO in GO and FGO. Triangles indicate the nucleolus or NLB. Scale bar, 20 μm. (g) Fluorescence of CYTO signal in HeLa cells treated with or without CX-5461 (1 μM) for 24 h. Scale bar, 20 μm. (h) Fluorescence of CYTO in HeLa cells treated with RNase A or both DNase I and RNase A. Scale bar, 10 μm. (i) Distribution of PQS (G-score ≥ 30) within mouse 47S pre-rRNA (Genebank: BK000964.3). (j) DNA sequences of PQS and representative mutants used for CYTO incubation and fluorescence spectra detection. (k) Fluorescence spectra of CYTO incubated with PQS and mutants listed in panel (j). Abbreviations: Relative Fluorescence Unit (RFU). (l) Biotin-labelled PQS (ITS1-Q1) and mutant sequence (ITS1-Q1-Mut) used for streptavidin pull-down assay. (m) Western blot analysis of DHX36 enriched by streptavidin-pull down assay. (n) Fluorescence of CYTO signal in WT and CKO FGO. Triangles indicate the NLBs of the cytoplasm of WT and CKO FGO. Data are presented as mean ± SEM. Unpaired t-tests were used for statistical analyses (d, o and p). *P < 0.05 and ***** P < 0.0001.

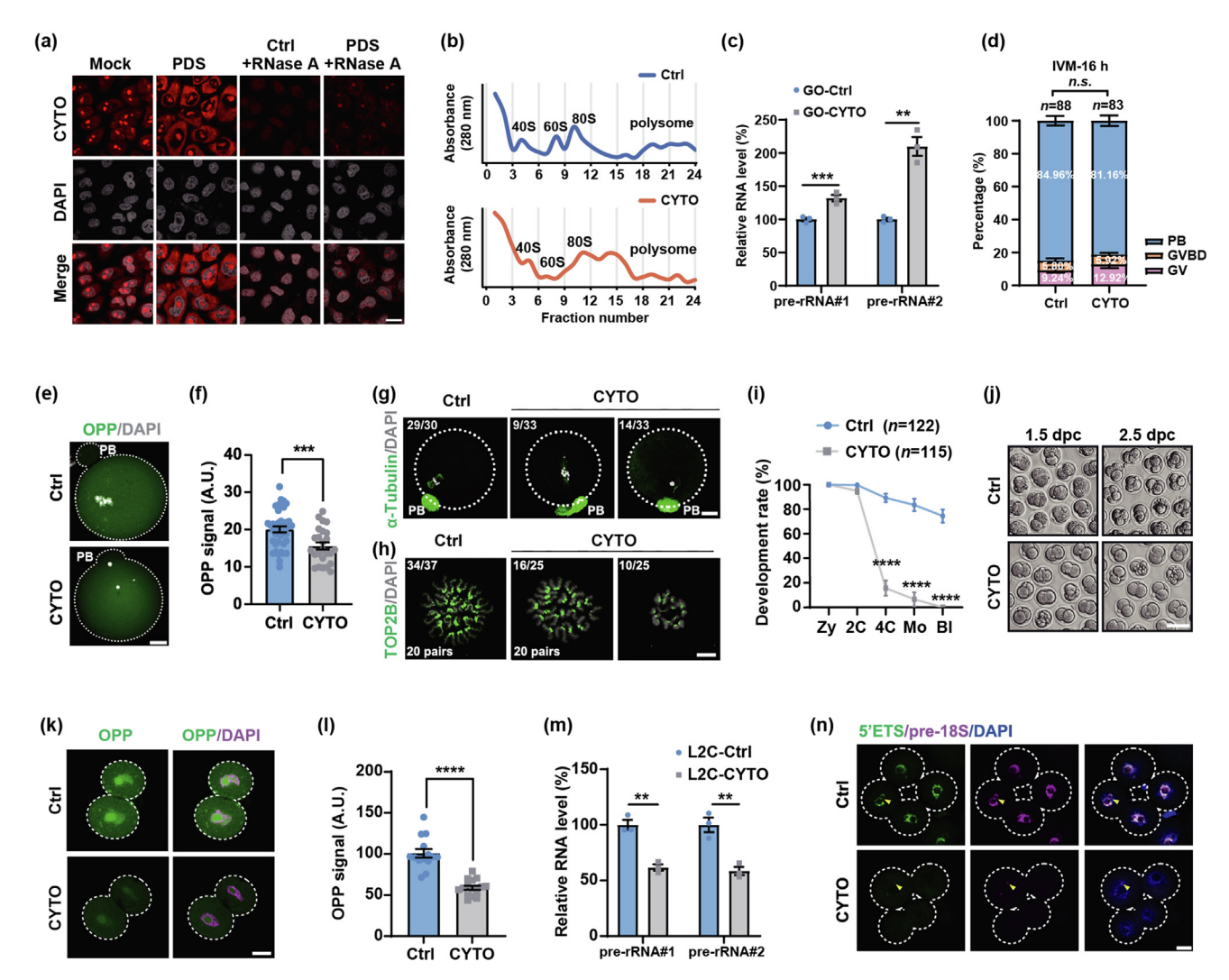


Fig. 7. G4s stabilization disrupts rRNA homeostasis. (a) Fluorescence of CYTO in HeLa cells treated with or without RNase A following 24 h of PDS (10 μ mol/L) treatment. Scale bar, 20 μ m. (b) Polysome profiles of MOSE cells treated with or without CYTO (50 nmol/L) for 24 h, analyzed by sucrose gradient fractionation. (c) qPCR analysis of pre-rRNA level in GO with or without CYTO treatment. (d) Proportion of oocytes with or without CYTO (50 nmol/L) treatment at IVM-16 h after IVM culture. (e) The OPP staining of oocytes at IVM-16 h. Scale bar, 20 μ m. (f) Quantification of OPP signal intensity in MII oocytes. (g) Immunofluorescence staining of α -Tubulin in oocytes. Scale bar, 100 μ m. (h) Immunofluorescence staining of TOP2B in chromatin spreading samples. Scale bar, 10 μ m. (i) Development rate of early embryos with or without CYTO (50 nmol/L) treatment during culture. (j) Images showing early embryos during *in vitro* culture. Scale bar, 100 μ m. (k) The OPP staining of L2C. Scale bar, 20 μ m. (l) Quantification of OPP intensity in L2C. (m) qPCR analysis of pre-rRNA level in L2C. (n) FISH showing pre-rRNA (5' ETS and pre-18S) signal in 4-cell. Scale bar, 20 μ m. Data are presented as mean \pm SEM. Unpaired *t*-tests (c, f, i, l and m) or a two-way ANOVA (d) were used for statistical analyses. P > 0.05 (n.s.), **P < 0.01, **P < 0.001 and ****P < 0.0001.

decreased pre-rRNA. The difference can be attributed to variations in primary rRNA transcription status at these developmental stages. Specifically, GO already exhibits active rRNA transcription prior to CYTO treatment, while rRNA transcription does not commence until the late 2-cell stage. Our findings indicate that CYTO primarily binds to pre-rRNA, as shown in Fig. 6h. Consequently, we hypothesize that CYTO predominantly inhibits the processing and splicing of pre-rRNA rather than affecting rRNA transcription in GO, resulting in an overall increase in pre-rRNA level post-treatment. In contrast, when CYTO was added from the zygote stage to 4-cell embryo stage—during which rRNA transcription is just gradually initializing—we observed a significant decrease in pre-rRNA level. The influence of G4s stabilizers on rRNA homeostasis may depend on both the basal transcription status of cells and

the stabilizers' preferential effects on pre-rRNA transcription and maturation.

Our study also reveals a correlation between DHX36, chromatin configuration, and chromatin accessibility. The abnormal chromatin configuration in CKO GV oocytes is characterized by decreased histone modifications and dispersed HP1 α distribution. The ATAC-seq revealed decreased chromatin accessibility at the TSS and rDNA region in CKO GV oocytes but increased enrichment of G4 motif in the open regions (Fig. 9c). The mechanisms by which DNA G4 formation potentially contributes to the observed abnormalities in chromatin configuration and histone modifications remain unclear, warranting further investigation. Our study provides important physiological insights that may inform future research in this area.

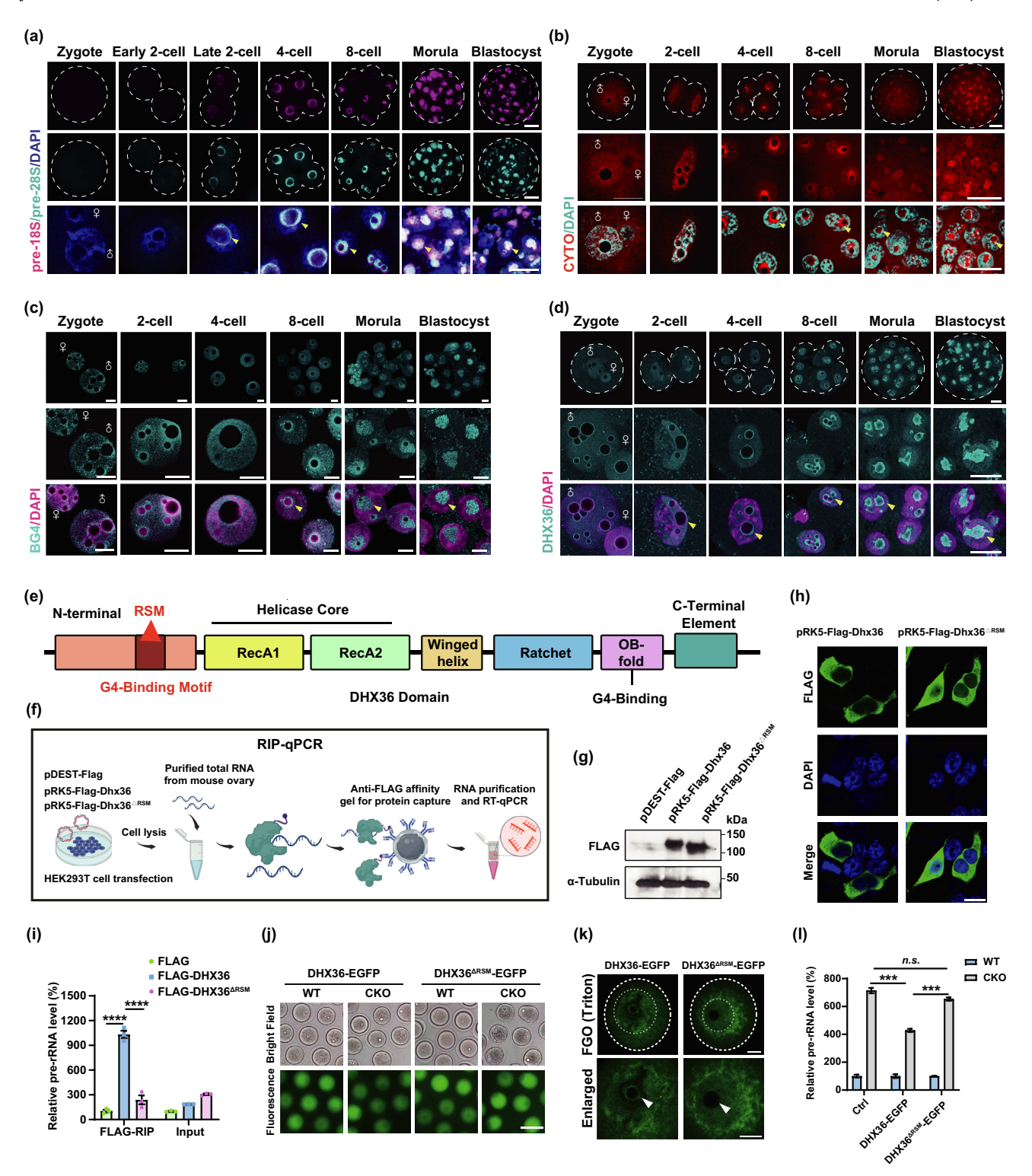


Fig. 8. Interaction between DHX36 and G4s on pre-rRNA. (a) FISH of pre-18S and pre-28S rRNA in mouse early embryos. Yellow triangles indicate pre-rRNA signal within the NPB or nucleolus. Scale bar, 20 μm. (b) Fluorescence of CYTO signal in mouse early embryos. Yellow triangles indicate the CYTO signal within the NPB or nucleolus. Scale bar, 20 μm. (c) BG4 signal detected in the chromatin spreading samples of mouse early embryos. Yellow triangles indicate BG4 signal within the NPB or nucleolus. Scale bar, 20 μm. (d) Immunofluorescence staining of DHX36 in mouse oocytes and early embryos. Yellow triangles indicate the DHX36 signal within the NPB or nucleolus. Scale bar, 20 μm. (e) Schematic representation of DHX36 protein domains. (f) Workflow diagram of the RIP-qPCR assay. (g) Western blot analysis of HEK293T cells transfected with pDEST-Flag-Dhx36 and pRK5-Flag-Dhx36^{ΔRSM}. (h) Immunofluorescence images of HEK293T cells transfected with pRK5-Flag-Dhx36 and pRK5-Flag-Dhx36^{ΔRSM}. Scale bar, 20 μm. (i) RIP-qPCR analysis of pre-rRNA level. (j) Images showing WT and CKO FGO overexpressed with DHX36-EGFP and DHX36^{ΔRSM}-EGFP following Triton treatment. White triangles indicate the NLBs. Scale bar, 20 μm. (l) qPCR analysis of pre-rRNA level in WT and CKO FGO overexpressed with either DHX36^{ΔRSM}-EGFP or DHX36^{ΔRSM}-EGFP. Data are presented as mean ± SEM. Unpaired *t*-tests were used for statistical analysis (i and l). ***P < 0.001, and ****P < 0.0001.

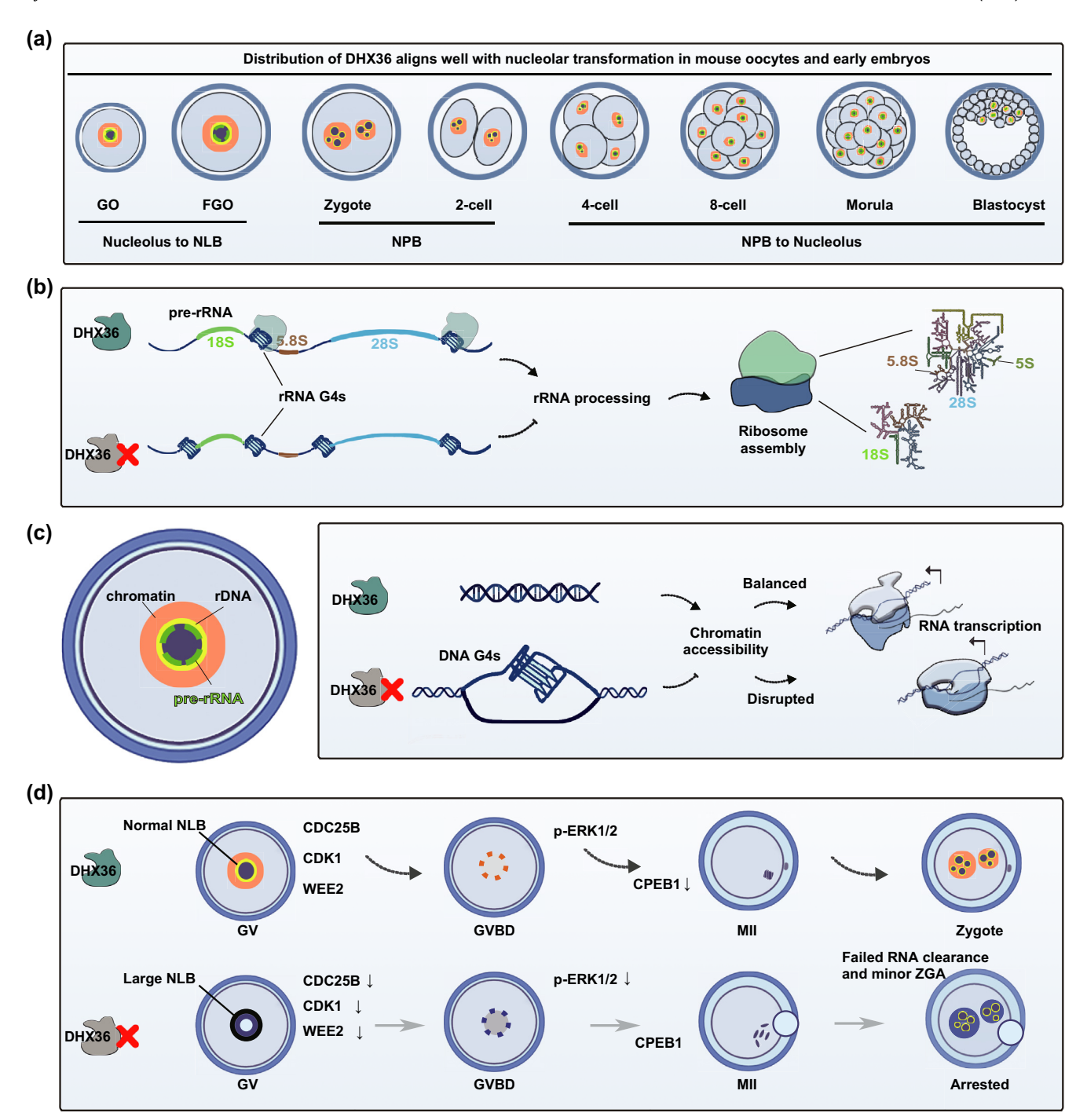


Fig. 9. DHX36-mediated regulation of G4s in DNA and pre-rRNA during mouse oocytes and early embryo development. (a) Spatiotemporal localization of DHX36 in mouse oocytes and early embryos coincides with pre-rRNA distribution and chromatin configuration transformations. (b) Accumulation of RNA G4s in pre-rRNA inhibits pre-rRNA processing and ribosome assembly in mouse GV oocytes. (c) Accumulation of DNA G4s decreases overall chromatin accessibility and disrupts mRNA and rRNA transcription in mouse GV oocytes. (d) In *Dhx36*-deficient oocytes, there are an inhibition of meiosis resumption and an arrest of early embryo development, accompanied by decreased expression levels of CDC25B, CDK1, and WEE2, reduced phosphorylation of ERK1/2, and accumulation of CPEB1.

In conclusion, these transcriptional and translational deficiencies, combined with inadequate expression of key meiosis-related proteins, lead to compromised meiosis resumption and poor early embryo development in CKO oocytes (Fig. 9d).

Conflict of interest

The authors declare that they have no conflict of interest.

Acknowledgments

This work was supported by the National Key Research and Development Program of China (2021YFC2700100), the National Natural Science Foundation of China (31930031 and 32300714), the Key Research and Development Program of Zhejiang Province, China (2021C03100 and 2021C03098), the Natural Science Foundation of Zhejiang Province, China (LD22C060001), and the

National Ten Thousand Talent Program, China. We thank the Confocal Imaging and Transmission Electron Microscopy Platform at the Life Sciences Institute, Zhejiang University for the technical assistance.

Author contributions

Heng-Yu Fan conceived and supervised this study. Yu-Xuan Jiao designed and performed the experiments, and wrote the manuscript. Guo-Wei Bu performed the ATAC-seq and RNA-seq. Yu-Wen Wu, Yu-Ke Wu, Bao-bao Chen, Meng-Ting She, Yi-Hang Zhang and Yu-ling Lu assisted with the experiments.

Data availability

The RNA-seq and ATAC-seq data were deposited in the NCBI Gene Expression Omnibus database with the GEO accession number of GSE266915 and GSE266885.

Appendix A. Supplementary material

Supplementary data to this article can be found online at https://doi.org/10.1016/j.scib.2025.02.017.

References

- Spiegel J, Adhikari S, Balasubramanian S. The structure and function of DNA Gquadruplexes. Trends Chem 2020;2:123–36.
- [2] Burge S, Parkinson GN, Hazel P, et al. Quadruplex DNA: sequence, topology and structure. Nucleic Acids Res 2006;34:5402–15.
- [3] Biffi G, Tannahill D, McCafferty J, et al. Quantitative visualization of DNA G-quadruplex structures in human cells. Nat Chem 2013;5:182–6.
- [4] Biffi G, Di Antonio M, Tannahill D, et al. Visualization and selective chemical targeting of RNA G-quadruplex structures in the cytoplasm of human cells. Nat Chem 2014;6:75–80.
- [5] Huppert JL, Balasubramanian S. Prevalence of quadruplexes in the human genome. Nucleic Acids Res 2005;33:2908–16.
- [6] Parkinson GN, Lee MP, Neidle S. Crystal structure of parallel quadruplexes from human telomeric DNA. Nature 2002;417:876–80.
- [7] Ambrus A, Chen D, Dai J, et al. Solution structure of the biologically relevant G-quadruplex element in the human c-MYC promoter. Implications for G-quadruplex stabilization. Biochemistry 2005;44:2048–58.
- [8] Rodriguez R, Miller KM, Forment JV, et al. Small-molecule-induced DNA damage identifies alternative DNA structures in human genes. Nat Chem Biol 2012;8:301–10.
- [9] Lefebvre J, Guetta C, Poyer F, et al. Copper-alkyne complexation responsible for the nucleolar localization of quadruplex nucleic acid drugs labeled by click reactions. Angew Chem Int Ed Engl 2017;56:11365–9.
- [10] Lu YJ, Yan SC, Chan FY, et al. Benzothiazole-substituted benzofuroquinolinium dye: a selective switch-on fluorescent probe for G-quadruplex. Chem Commun (Camb) 2011;47:4971–3.
- [11] Laguerre A, Hukezalie K, Winckler P, et al. Visualization of RNA-quadruplexes in live cells. J Am Chem Soc 2015;137:8521–5.
- [12] Chen MC, Tippana R, Demeshkina NA, et al. Structural basis of G-quadruplex unfolding by the DEAH/RHA helicase DHX36. Nature 2018;558:465–9.
- [13] Giri B, Smaldino PJ, Thys RG, et al. G4 resolvase 1 tightly binds and unwinds unimolecular G4-DNA. Nucleic Acids Res 2011;39:7161–78.
- [14] Chen MC, Murat P, Abecassis K, et al. Insights into the mechanism of a G-quadruplex-unwinding DEAH-box helicase. Nucleic Acids Res 2015;43:2223–31.
- [15] Zhang K, Zhang T, Zhang Y, et al. DNA/RNA helicase DHX36 is required for late stages of spermatogenesis. | Mol Cell Biol 2023;14:mjac069.
- [16] Gao X, Ma W, Nie J, et al. A G-quadruplex DNA structure resolvase, RHAU, is essential for spermatogonia differentiation. Cell Death Dis 2015;6:e1610.
- [17] Nie J, Jiang M, Zhang X, et al. Post-transcriptional regulation of Nkx2-5 by RHAU in heart development. Cell Rep 2015;13:723–32.
- [18] Kresoja-Rakic J, Santoro R. Nucleolus and rRNA gene chromatin in early embryo development. Trends Genet 2019;35:868–79.

- [19] Bogolyubov DS. Karyosphere (Karyosome): a peculiar structure of the oocyte nucleus. Int Rev Cell Mol Biol 2018;337:1–48.
- [20] Bogolyubova I, Bogolyubov D. Heterochromatin morphodynamics in late oogenesis and early embryogenesis of mammals. Cells 2020;9:1497.
- [21] Fulka H, Langerova A. Nucleoli in embryos: a central structural platform for embryonic chromatin remodeling? Chromosome Res 2019;27:129–40.
- [22] Booy EP, Howard R, Marushchak O, et al. The RNA helicase RHAU (DHX36) suppresses expression of the transcription factor PITX1. Nucleic Acids Res 2014;42:3346-61.
- [23] Picelli S, Faridani OR, Bjorklund AK, et al. Full-length RNA-seq from single cells using Smart-seq2. Nat Protoc 2014;9:171–81.
- [24] George SS, Pimkin M, Paralkar VR. Construction and validation of customized genomes for human and mouse ribosomal DNA mapping. J Biol Chem 2023;299:104766.
- [25] Kikin O, D'Antonio L, Bagga PS. QGRS Mapper: a web-based server for predicting G-quadruplexes in nucleotide sequences. Nucleic Acids Res 2006;34:W676–82.
- [26] Duncan FE, Jasti S, Paulson A, et al. Age-associated dysregulation of protein metabolism in the mammalian oocyte. Aging Cell 2017;16:1381–93.
- [27] Feng Y, Guo L, Yang C, et al. The local density of H3K9me3 dictates the stability of HP1alpha condensates-mediated genomic interactions. J Genet Genomics 2023;50:776–85.
- [28] Larson AG, Elnatan D, Keenen MM, et al. Liquid droplet formation by HP1alpha suggests a role for phase separation in heterochromatin. Nature 2017;547:236–40.
- [29] Hansel-Hertsch R, Spiegel J, Marsico G, et al. Genome-wide mapping of endogenous G-quadruplex DNA structures by chromatin immunoprecipitation and high-throughput sequencing. Nat Protoc 2018;13:551–64.
- [30] Kalous J, Tetkova A, Kubelka M, et al. Importance of ERK1/2 in regulation of protein translation during oocyte meiosis. Int J Mol Sci 2018;19:698.
- [31] Zhang YL, Liu XM, Ji SY, et al. ERK1/2 activities are dispensable for oocyte growth but are required for meiotic maturation and pronuclear formation in mouse. J Genet Genomics 2015;42:477–85.
- [32] Zhang C, Chen Z, Yin Q, et al. The chromatin remodeler Snf2h is essential for oocyte meiotic cell cycle progression. Genes Dev 2020;34:166–78.
- [33] Walser CB, Lipshitz HD. Transcript clearance during the maternal-to-zygotic transition. Curr Opin Genet Dev 2011;21:431–43.
- [34] Schofer C, Weipoltshammer K. Nucleolus and chromatin. Histochem Cell Biol 2018;150:209–25.
- [35] Mullineux ST, Lafontaine DL. Mapping the cleavage sites on mammalian prerRNAs: where do we stand? Biochimie 2012;94:1521–32.
- [36] Fouquerel E, Parikh D, Opresko P. DNA damage processing at telomeres: the ends justify the means. DNA Repair (Amst) 2016;44:159–68.
- [37] Amato J, Madanayake TW, Iaccarino N, et al. HMGB1 binds to the KRAS promoter G-quadruplex: a new player in oncogene transcriptional regulation? Chem Commun (Camb) 2018;54:9442-5.
- [38] Fleming AM, Ding Y, Burrows CJ. Oxidative DNA damage is epigenetic by regulating gene transcription via base excision repair. Proc Natl Acad Sci USA 2017;114:2604–9.
- [39] Shen J, Varshney D, Simeone A, et al. Promoter G-quadruplex folding precedes transcription and is controlled by chromatin. Genome Biol 2021;22:143.
- [40] Paeschke K, Bochman ML, Garcia PD, et al. Pif1 family helicases suppress genome instability at G-quadruplex motifs. Nature 2013;497:458–62.
- [41] Zyner KG, Simeone A, Flynn SM, et al. G-quadruplex DNA structures in human stem cells and differentiation. Nat Commun 2022;13:142.
- [42] Lopes J, Piazza A, Bermejo R, et al. G-quadruplex-induced instability during leading-strand replication. EMBO J 2011;30:4033–46.
- [43] Sauer M, Juranek SA, Marks J, et al. DHX36 prevents the accumulation of translationally inactive mRNAs with G4-structures in untranslated regions. Nat Commun 2019:10:2421.
- [44] Yoo JS, Takahasi K, Ng CS, et al. DHX36 enhances RIG-I signaling by facilitating PKR-mediated antiviral stress granule formation. PLoS Pathog 2014;10: e1004012.
- [45] Lai JC, Ponti S, Pan D, et al. The DEAH-box helicase RHAU is an essential gene and critical for mouse hematopoiesis. Blood 2012;119:4291–300.
- [46] Mestre-Fos S, Penev PI, Suttapitugsakul S, et al. G-quadruplexes in human ribosomal RNA. J Mol Biol 2019;431:1940–55.
- [47] Mestre-Fos S, Penev PI, Richards JC, et al. Profusion of G-quadruplexes on both subunits of metazoan ribosomes. PLoS One 2019;14:e0226177.
- [48] Mestre-Fos S, Ito C, Moore CM, et al. Human ribosomal G-quadruplexes regulate heme bioavailability. J Biol Chem 2020;295:14855–65.
- [49] Wang H, Gu Y, Shen X, et al. Selection and expression profiles of reference genes in mouse preimplantation embryos of different ploidies at various developmental stages. PLoS ONE 2014;9:e98956.